RADIATION RESEARCH **154**, 564–581 (2000)
0033-7587/00 $5.00

Measurement and Validation of Benchmark-Quality Thick-Target Tungsten X-Ray Spectra below 150 kVp

J. R. Mercier,[a,1] D. T. Kopp,[a] W. D. McDavid,[b] S. B. Dove,[b] J. L. Lancaster[c] and D. M. Tucker[d]

[a] *The University of Texas Health Science Center at San Antonio, Radiological Sciences Division, San Antonio, Texas 78284-7800;* [b] *The University of Texas Health Science Center at San Antonio, Dental Diagnostic Sciences Division, San Antonio, Texas 78284-7919;* [c] *The University of Texas Health Science Center at San Antonio, Research Imaging Center, San Antonio, Texas 78284-6239; and* [d] *Storage Technology Corporation, Louisville, Colorado 80028-8102*

Mercier, J. R., Kopp, D. T., McDavid, W. D., Dove, S. B., Lancaster, J. L. and Tucker, D. M. Measurement and Validation of Benchmark-Quality Thick-Target Tungsten X-Ray Spectra below 150 kVp. ***Radiat. Res.*** **154, 564–581 (2000).**

Pulse-height distributions of two constant potential X-ray tubes with fixed anode tungsten targets were measured and unfolded. The measurements employed quantitative alignment of the beam, the use of two different semiconductor detectors (high-purity germanium and cadmium-zinc-telluride), two different ion chamber systems with beam-specific calibration factors, and various filter and tube potential combinations. Monte Carlo response matrices were generated for each detector for unfolding the pulse-height distributions into spectra incident on the detectors. These response matrices were validated for the low error bars assigned to the data. A significant aspect of the validation of spectra, and a detailed characterization of the X-ray tubes, involved measuring filtered and unfiltered beams at multiple tube potentials (30–150 kVp). Full corrections to ion chamber readings were employed to convert normalized fluence spectra into absolute fluence spectra. The characterization of fixed anode pitting and its dominance over exit window plating and/or detector dead layer was determined. An Appendix of tabulated benchmark spectra with assigned error ranges was developed for future reference.

INTRODUCTION

One of the many factors that influences the ability of the radiologist to detect subtle lesions in X-ray-based imaging is the signal-to-noise ratio presented by the lesion in the image. This important factor ultimately depends on the spectrum of the X-ray beam incident on the patient for the imaging procedure. Establishing imaging techniques that yield incident spectra that optimize the relationship between the dose to the patient and image quality involves modeling the X-ray imaging chain from the point of production of the primary beam in the anode to absorption of primary and secondary radiation in a specific image receptor. Therefore, knowledge of the X-ray spectrum is paramount in image optimization.

Validation of any spectral model for predicting tungsten X-ray tube spectra requires agreement between the calculated spectra and benchmark-quality measured spectra across the range of applications for which it is intended to simulate. A robust and powerful technique that can be used for modeling X-ray spectra is with the Monte Carlo method for simulating coupled electron–photon radiation transport. For X-ray spectra to be of benchmark quality for validating a Monte Carlo code, or other computational methods, they must be accurate, reproducible and well documented. Although Profio (*1*) makes some suggestions for recording benchmark-quality measured data, such as sketching and describing the experimental setup, the following guidelines were found useful for ongoing research. Beams must be characterized in detail for geometry and composition of anode, for detectors, and for inherent and added filtration. Waveforms for voltage (in kV) and current (in mA) should be described. Other information pertinent to the Monte Carlo modeling process, such as assessments of anode pitting and detector dead layer, should be provided. Beam alignment and scatter reduction techniques should be presented. A thorough error analysis of the measured data is required, and any databases used in calculations (e.g. attenuation and energy absorption coefficients) should be referenced. Calibration and quality control of the spectroscopy system should be discussed, and ion chamber corrections (e.g. for energy response, temperature, pressure) should be presented. The method for unfolding X-ray pulse-height distributions into spectra must be described and validated. Finally, the benchmark data should be provided in tabulated form and presented in a peer-reviewed scientific journal for use by others.

Although several scientific papers and a few government reports have presented measured tungsten spectra (*2–12*), none of them appear to meet all the stringent benchmarking requirements of a Monte Carlo code. This paper, supported

[1] Author to whom correspondence should be addressed at 8500 Chapel Drive, Annandale, VA 22003.

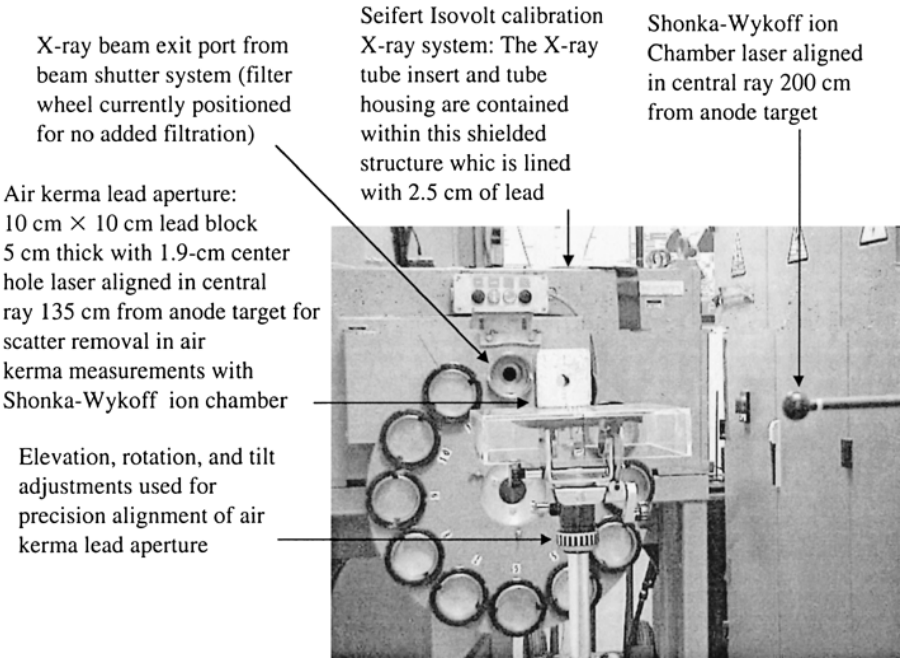

FIG. 1. Seifert isovolt calibration X-ray system. The experimental arrangement depicts the setup configuration for air kerma measurement.

with more detail in the primary author's Ph.D. dissertation,[2] is intended to fill that void for tungsten spectra in the range of 30–150 kVp.

EXPERIMENTAL DETAILS

Summary of Experimental Techniques

For collecting, correcting and interpreting experimental spectral data, this study introduces several new techniques and implements numerous methods previously demonstrated by others. Much like the classic work of Hettinger and Starfelt (*6*), we use a series of shielded apertures and pinhole collimators aligned with the central ray of the beam to gather pulse-height distributions of filtered and unfiltered spectra at different tube potentials. To limit pulse pileup in the spectroscopy system and to ensure that only the primary beam is measured, the beam is tightly confined and collimated to 100 μm in diameter at a distance of 350 cm from the target. This very narrow beam is aligned quantitatively for high precision and repeatability. Spectroscopy measurements were acquired during continuous beam-on operation and employed intrinsic high-purity germanium and cadmium-zinc-telluride ($C_{0.9}Z_{0.1}T$) semiconductor crystals. Detector-dependent Monte Carlo response matrices were generated for unfolding the pulse-height distributions into spectra incident on the detectors. Comprehensive validation of the unfolding method was achieved by comparing measured filtered spectra to measured unfiltered spectra that have been filtered analytically. Scaling normalized spectra to give air kerma values in agreement with measured ion chamber readings provided absolute photon fluence and air kerma spectra. Two different ion chambers were used under low scatter conditions for air kerma measurements. Standard corrections (e.g. pressure and temperature) as well as beam-specific calibration factors were applied to ion chamber readings. Anode pitting was assessed for full characterization of the beams in which benchmark spectra were recorded.

X-Ray Generators and Tubes

The majority of data acquired in this study came from measurements of X-ray beams produced by a Seifert Isovolt DS1D three-phase calibration system with a metal ceramic MB 420/1 X-ray tube insert and 420/10 tube housing (Fig. 1). As the name implies, the Isovolt unit maintains a nearly constant potential (<2% ripple) voltage waveform. The nearly flat waveforms are accomplished in this three-phase calibration system through additional capacitance smoothing circuits not found in clinical systems. Similar smoothing is provided in the filament circuit so that the milliamp (mA) waveform is nearly that of direct current (<2% ripple). Unlike most systems, the actual kilovolt peak (kVp) and current (mA) across the tube during an exposure are monitored within the generator and conveniently displayed at the control panel. The thick tungsten ($Z = 74$) anode target is >99.9% pure and is embedded in a large copper heat sink that is water-cooled. The anode target angle is 20°. The beam is modified by a total of 7 mm beryllium inherent filtration which results from a 4-mm-thick beryllium anode port and a 3-mm-thick beryllium exit port. The tube housing is mounted in a large shielded structure that also supports a filter wheel and beam shutter system. For the narrow beam geometry previously specified, dead time in the spectroscopy system is kept under 2% with tube currents in the range of 0.5–10 mA.

The second X-ray system used in this study was a high-frequency Siemens Heliodent MD unit with an SR 60/70/7 tube. This dental X-ray unit can be operated at 60 or 70 kVp at a fixed current of 7 mA. The voltage and current waveforms for this system are also nearly constant potential and direct current, respectively. The anode angle is 12° and the fixed anode target is >99.9% pure tungsten. The inherent filtration in this unit consists of 0.8 mm of X-ray tube glass, 15 mm of electric insulating oil, and 1.3 mm of aluminum. The glass, insulating oil and aluminum densities are 2.23, 0.866 and 2.699 g/cm^3, respectively. The oil and tube glass can be modeled effectively for elemental composition as polyethylene (CH_2) and Pyrex glass, respectively. Dead time in the spectroscopy system was about 1% at both kVp settings for the narrow beam geometry previously specified.

Since the output X-ray beam waveform is a function of voltage and

[2] For more detailed discussions, refer to J. R. Mercier, ''Measurement and Monte Carlo Prediction of Diagnostic Tungsten X-Ray Spectra,'' Ph.D. Dissertation, Graduate School of Biomedical Sciences, The University of Texas Health Science Center, San Antonio, TX, 1999. Available from UMI Dissertation Services, Ann Arbor, MI, 1999, UMI No. 9938769.

current waveforms, a small silicon diode array connected to an oscilloscope was used to verify the ripple content of the output beam. The diode detector provides an instantaneous current output signal when subjected to the X-ray beam. For the full range of voltages (30 to 150 kVp) and currents (0.5 to 10 mA) used in this study, there was no appreciable ripple measured in the output beams for either X-ray system. The diode detector was also used to assess X-ray shutter timer error and verify exposure timer accuracy.

Spectroscopy System and Detectors

With their high-resolution capability and linear energy response, semiconductor detectors have proven to be the detectors of choice for measuring spectra in the diagnostic energy range. Whether intrinsic or the older lithium-drifted type, germanium semiconductor detectors have provided the best spectral results over the last three decades and therefore are the current standard. The most recent low-energy γ- and X-ray spectroscopy challenger to intrinsic germanium is cadmium-zinc-telluride. This study employs both high-purity germanium- and cadmium-zinc-telluride-type detectors with 60 keV line-energy system resolutions of roughly 1.5 and 3.0 keV (peak full width at half-maximum), respectively.

Detector signals are modified and enhanced as they pass through a sophisticated electronic spectroscopy system to form pulse-height distributions in a multichannel analyzer. An oscilloscope is used to ensure proper setup and signal flow at each step in the system. Calibration of the 0.5 keV channel widths was performed with ^{241}Am and ^{57}Co sources. System calibration was very stable so that a single energy calibration was usually sufficient on any given day.

The primary detector for collecting pulse-height distributions of incident spectra was a reverse-electrode coaxial intrinsic high-purity germanium detector. The high-purity germanium crystal is mounted behind a 0.5-mm-thick beryllium window in an evacuated aluminum cryostat housing atop a copper cold finger for liquid nitrogen cooling. The high-purity germanium crystal is cylindrical with a diameter of 49.5 mm. The crystal is only 14.5 mm thick out to a centerline radius of 3.75 mm and is 50.5 mm thick elsewhere. In high-purity germanium detectors, the contacts are made of diffused lithium in the N-type layer and boron-ion implantation in the P-type layer. In a standard coaxial design, the P-type contact is 2–3 μm thick and lines the crystal at the inner void area and the much thicker (~500 μm) N-type contact covers the front face and sides of the crystal. An advantage of the reverse-electrode detector design used for this study is that the locations of the P and N contacts are reversed so that the detector dead layer is all but eliminated (e.g. 3 compared to 500 μm). The spectroscopy system was configured for interchanging the high-purity germanium and cadmium-zinc-telluride detectors. The cadmium-zinc-telluride crystal is only 2 mm thick, has a 3 × 3-mm face, and is mounted on a tiny thermoelectric cooler. The cadmium-zinc-telluride detector beryllium window is 250 μm thick.

Ion Chambers

For high accuracy, the superbly designed and time-tested Shonka-Wykoff ion chamber (Fig. 1) was used for measuring air kerma of primary X-ray beams (*13*). The Shonka-Wykoff chamber was calibrated at the National Institute of Standards and Technology (NIST) in which air kerma calibration factors in grays per coulomb (Gy/C) were provided in a calibration report for various NIST beam codes. The calibration factors are accurate to 1% with a 95% confidence interval.

A second well-designed ion chamber system was employed to measure air kerma in the beams. This was an MDH 1015 series monitor with 10X5-6 and 10X5-6M probes (*14*). The MDH calibration was performed by the Food and Drug Administration (FDA) and is traceable to NIST. The accuracy for this calibration was 5%. MDH exposure rate readings were converted to air kerma values and used as a general check on the values obtained with the Shonka-Wykoff chamber.

UNFOLDING OF HIGH-PURITY GERMANIUM SPECTRA

Although high-purity germanium detectors have the advantage of high resolution with reasonably high detection efficiencies, it is still necessary to correct the measured pulse-height distributions for the distorting effects of the detector response. Except for recourse to rather crude approximations, estimation of the Compton continua and the corresponding full-energy absorption probabilities has depended on Monte Carlo calculations (*15*). Incorporating the performance characteristics of the detector in relation to crystal geometry, beam geometry, and beam energy is important for achieving the best results. Using version 4B2 of the Monte Carlo N-Particle (MCNP4B2) radiation transport code (*16*), detector response was modeled for a very narrow beam normally incident on the face of the detector. Monte Carlo and analytical modeling of detector response and spectra unfolding procedures are introduced in refs. (*5, 7, 10, 15*).

For a full-scatter structure, the modeling included the beryllium window, the previously described crystal geometry, the aluminum cryostat housing, an estimate of various backing materials beyond the crystal, and the head of the copper cold finger. Figure 2 shows the predicted response for 155 keV monoenergetic beams at the center of the detector and 1 cm off center. The figure also shows the detector response for Monte Carlo modeling of just the beryllium window and the bare crystal for the 1-cm off-center beam. The backscatter peak with an edge at 155 – 58.5 = 96.5 keV is correctly shown for the centerline beam and is absent for the off-center beam, where the crystal is sufficiently thick that only a small percentage of the beam is transmitted. The nearly full absorption condition is also explicative of the agreement between the bare detector and full scatter modeling in the off-center beam.

Monte Carlo and photopeak efficiency curves calculated analytically for the high-purity germanium crystal are shown in Fig. 3 for energies up to 150 keV. Following Israel *et al.* (*7*), the analytical calculation is a simple exponential attenuation calculation using the narrow-beam total energy absorption coefficient for germanium and the total linear attenuation coefficient for beryllium. The analytical calculation does not account for the discontinuity at the crystal K-shell edge, the loss of K-shell X rays and Compton X rays from the front face and sides of the crystal, coherent scatter, or multiple scattered Compton X rays that affect the photopeak efficiency. Since the Monte Carlo calculation accounts for all of the important physical processes and for actual detector geometry, it is the method of choice for correcting measured data. Figure 3 shows that an off-center beam requires less full-energy response correction than a centerline beam for the coaxial detector geometry. In fact, application of off-center photopeak efficiency curves, which are above 90% and relatively flat across the energy range of interest, will result in little change in the

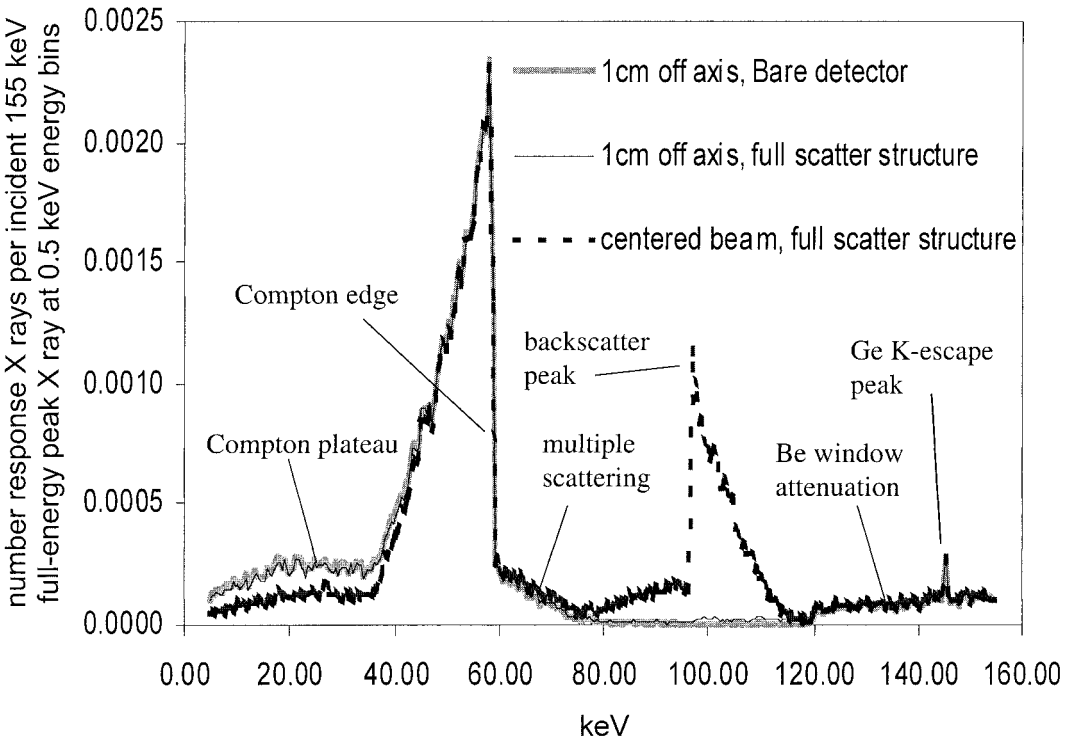

FIG. 2. Detector response. Monte Carlo-predicted high-purity germanium coaxial detector response to a very narrow 155 keV normally incident beam. Each Compton continuum starts at low energy and leads up to the Compton edge, which is given at 58.5 keV. Multiple scattering with eventual X-ray escape is shown above the Compton edge up to ~75 keV. Response for backscatter events follows at 75–120 keV. The result of beryllium window attenuation in the response curve comes from window scatter events that are most evident in the crystal in the 120–154.5 keV range. Superimposed on the window attenuation response is the germanium K-shell escape peak, which is at 145 keV (i.e. germanium characteristic K-shell radiation energy is about 10 keV). At centerline, about 26% of the beam is transmitted for subsequent interaction in the structure beyond the crystal. The backscatter peak with an edge at 155 – 58.5 = 96.5 keV is shown for the centerline beam, and it is absent for the off-center beam, where the crystal is sufficiently thick that only a small percentage of the beam is transmitted. The full energy peak, which would dwarf the rest of the response data, is excluded.

normalized shape of the measured spectra. Hence the off-center beam geometry was chosen for collecting spectral pulse-height distributions because it eliminates backscattering corrections (Fig. 2) and minimizes full-energy peak corrections (Fig. 3) for the energies of interest in this study.

Monte Carlo simulations were carried out for narrow monoenergetic beams incident normally to the detector face at a radius of 1 cm from the crystal centerline. The simulations were conducted for the energy range of 0–155 keV in increments of 0.5 keV. For every simulation, the data represented in Figs. 2 and 3 were tallied in intervals of 0.5 keV. The collective response estimate of all the simulations formed a large detector response matrix (310 × 310) that is used in a spreadsheet for unfolding the pulse-height distributions into incident spectra. Minor scaling of the response matrix as a function of energy was then employed for the best unfolding results of heavily filtered spectra. This matrix scaling technique avoids over- and undercorrection to the pulse-height distributions and is equivalent in concept to Seelentag and Panzer's scaling of the analytical Compton correction factor (*10*). Detector response matrix scaling is a good way to compensate for minor discrepancies between the actual physical world and the Monte Carlo modeling process.

After matrix unfolding, the K_α, K_β and L-shell characteristic peaks were stripped manually from the continuum. The K_α peak is split into $K_{\alpha 1}$ and $K_{\alpha 2}$ delta functions according to energies and the yield ratio for those peaks given in the 1997 Evaluated Atomic Data Library (EADL) (*17*). The $K_{\alpha 1}$ and $K_{\alpha 2}$ delta functions are then added back to the continuum at the energies given in the EADL. This peak stripping procedure is also applied in determining $K_{\beta 1}$, $K_{\beta 2}$, L_α and L_β delta functions for superposition on the continuum. Any noticeable K-shell edge aperture distortion, which is described by Fewell and Shuping (*4*), was stripped from the continuum and discarded.

Once pulse-height distributions are corrected for detector distortions and the spectra incident on the detector are unfolded, air attenuation is removed to a target distance of 2 m and the spectra are normalized to an area of 1. It is at this distance that primary-beam air kerma data were collected and used to convert normalized spectra into absolute fluence and kerma spectra.

Acquisition and correction of cadmium-zinc-telluride

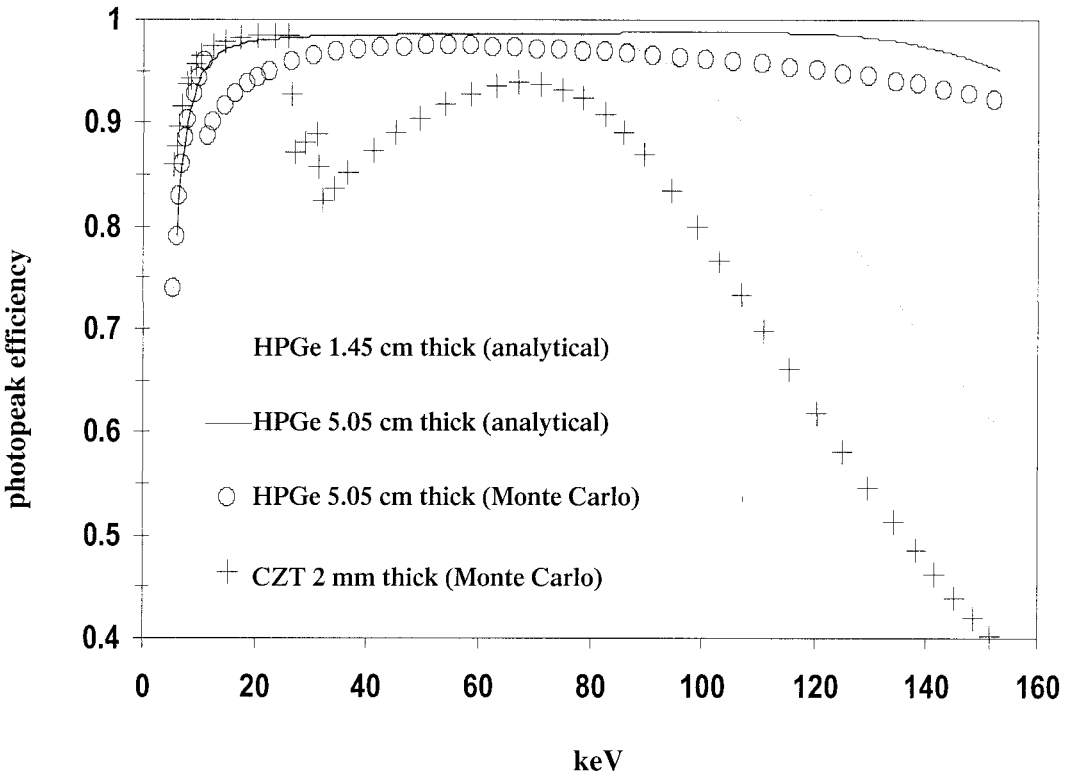

FIG. 3. Photopeak efficiency curves for high-purity germanium and cadmium-zinc-telluride detectors. The high-purity germanium analytical curves indicate that the 5.05-cm-thick off-center section of the coaxial detector will preserve the spectrum shape much better than the 1.45-cm-thick central section of the crystal. Therefore, the experimental arrangement and the superior Monte Carlo calculation of detector response were based on the narrow beam striking the detector at the thicker section. Although it is a higher average *Z* material, the thin cadmium-zinc-telluride detector requires much more photopeak efficiency correction to the pulse height distribution than does the high-purity germanium detector.

pulse-height distributions follow almost the same procedures as described for the high-purity germanium detector. The energy broadening for the cadmium-zinc-telluride detector took the form of a Gaussian with dramatic low-energy tail skewing. Thus far, a function has not been fitted for cadmium-zinc-telluride energy broadening. As a result, stripping of K-shell peaks has proven difficult and unreliable. Therefore, comparing high-purity germanium and cadmium-zinc-telluride spectra has been limited to tube potentials below 70 kVp.

QUANTITATIVE BEAM ALIGNMENT

Early experiments showed that unless extraordinary care is taken with respect to the collimation of the beam in the energy region of diagnostic X rays, the desired true spectrum will not be observed and spectral measurements cannot be reproduced (*3*). In all known instances, past experimentalists relied on some form of subjective optical technique for beam alignment with small apertures. In some cases, researchers reported the repeatability of their spectral measurements in the range of 5–20% (*2, 7*). In the present study, a laser optical system was designed for use in quantitatively aligning the X-ray beam from the point of origin at the anode focal spot, through a series of pinhole apertures, to a pinpoint location on the face of the detector (Fig. 4). This alignment technique yielded spectral pulse-height distributions with a repeatability of 1–2%.[2]

AIR KERMA MEASUREMENTS

The Shonka-Wykoff chamber was laser-aligned in the central ray 200 cm from the Seifert X-ray tube target for air kerma measurements (Fig. 1). At 200 cm, distance accuracy is within 0.25% and the central beam is uniform across the field of view presented by the ion chamber. Although the beam is already well collimated at the beam port exit, a reduction in air scatter of 1–1.5% was realized with additional collimation in the form of a lead brick with a 2-cm-diameter central hole placed 135 cm from the anode target. This collimation reduced the primary beam diameter at the chamber location from ~20 cm to ~3 cm for a low-scatter arrangement consistent with measurement of only the primary beam. Similar measurements were made with the larger MDH chambers, except that a brick with a 5-cm-diameter hole was used.

Shonka-Wykoff chamber calibration factors were determined for each beam. From NIST calibration, air kerma calibration factors (Gy/C) were known for NIST beam codes M30, M50, M60, M100, M150 and H150 (*18*). For

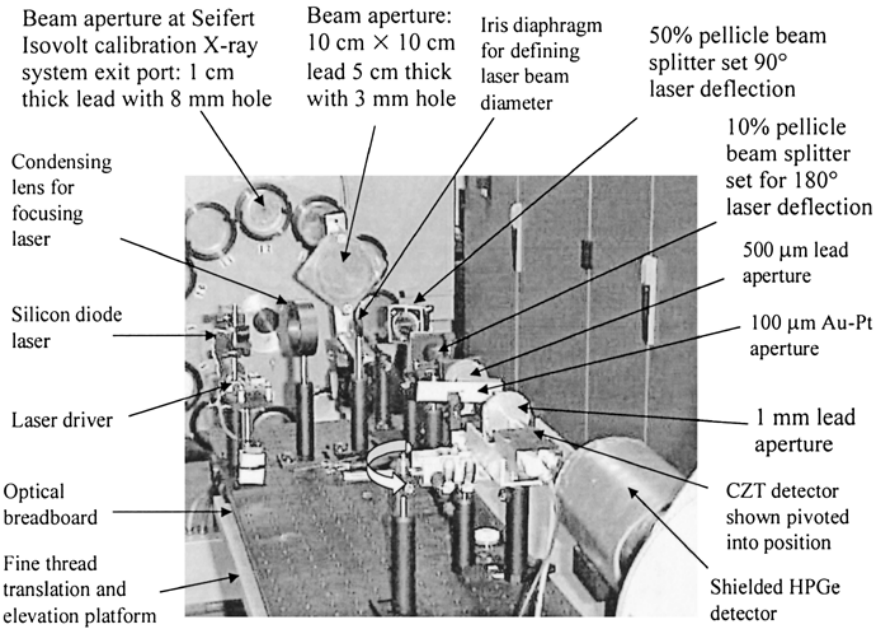

FIG. 4. Spectroscopy experimental arrangement. Centrally featured is the laser beam alignment system. The filter wheel for the Seifert Isovolt calibration X-ray system is in the background and the cadmium-zinc-telluride and high-purity germanium detectors are in the foreground.

the M60 and higher beam codes, the X-ray tube used at NIST to calibrate the Shonka-Wykoff chamber was made by the same manufacturer and identical in design (e.g. same anode composition, anode angle, and beryllium window thickness) to the tube installed in the Seifert system used for this study. For these beams, NIST spectra should be almost identical to the spectra measured here.

Chamber calibration factors for spectra at tube potentials and at filtrations differing from the beam codes noted were calculated by interpolation of the NIST calibration factors available. The standard method for such interpolation is by estimation from a plot of known calibration factors as a function of beam half-value thickness in aluminum or copper (*18, 19*). However, a more accurate method of calculating beam-specific (i.e. specific to each spectrum measured) calibration factors was developed and is described in detail elsewhere.[2]

In a few instances, the tube potential applied in spectral measurements differed slightly, but within 1.5 kVp, from that applied in the air kerma measurements. To account for these differences, the air kerma values were corrected for dependence on kVp.[2] The impact of kVp dependence corrections to air kerma quantities was typically less than 1% and never exceeded 2%. Shonka-Wykoff chamber readings received standard corrections for pressure, temperature, shutter timer error, and electrometer calibration factor (*20*). For all air kerma measurements, a concerted attempt was made to exactly reproduce the system parameters used to collect spectra (e.g. kVp, mA, filtration).

CALCULATING ABSOLUTE SPECTRA

The 2-m air kerma values were used to convert the unfolded normalized fluence spectra into absolute fluence and kerma spectra. Normalized fluence spectra can be described by

$$\int_0^E n(e)\, de = 1, \tag{1}$$

where $n(e)$ represents the fraction of X rays at energy e in the spectrum and E represents the maximum X-ray energy in the spectrum, which, of course, corresponds to the kVp applied across the X-ray tube. An absolute fluence spectrum with a total fluence of Φ [X rays/(cm^2-mAs)] is then given by

$$\int_0^E \Phi \cdot n(e)\, de = \Phi. \tag{2}$$

An absolute air kerma spectrum with a total kerma rate of X (Gy/mAs) is given by

$$X = \int_0^E \Phi \cdot \left[\frac{\mu_{en}(e)}{\rho}\right]_{\text{air}} \cdot e \cdot n(e)\, de. \tag{3}$$

In discrete form, Eq. (3) becomes

$$X = \sum_{i=0}^{E/\Delta e} \Phi \cdot \left[\frac{\mu_{en}(e)}{\rho}\right]_{\text{air}} \cdot e \cdot N_i(e) \cdot \Delta e, \tag{4}$$

where $N_i(e)$ is the fraction of X rays sampled at energy e in bin number i per energy bin of width Δe. The 0.5-keV energy bins (Δe) used in spectral acquisition and unfolding were also used to increment the summation. The Eq. (4) discrete form for air kerma was implemented in a spreadsheet. In the summation, e represented the mid-bin energy and Φ was varied to give the proper scaling of the normalized fluence spectrum so that the summation of the ab-

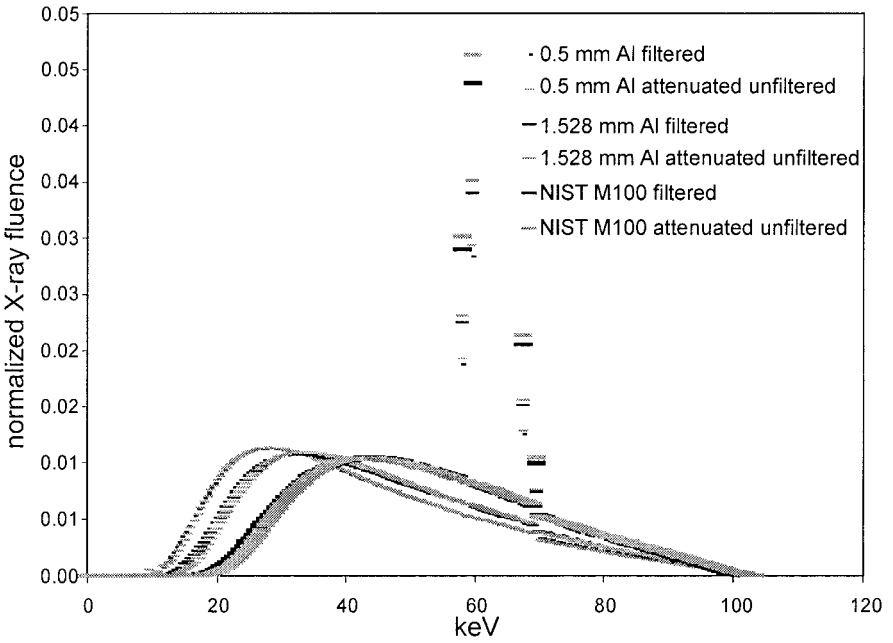

FIG. 5. Comparison of attenuated unfiltered spectra with filtered spectra at 101.5 kVp. Normalized unfiltered X-ray fluence spectrum attenuated to same filtration as companion unfolded filtered spectra for Seifert Isovolt system operating at 101.5 kVp. Each spectrum was normalized to an area of 1.0 in fluence units of X rays/(mAs·cm²) at a 1-m distance from the tungsten anode target. Inset indicates added filtrations.

solute kerma spectrum agreed with the actual measured air kerma value. The mass-energy absorption coefficients for air were derived from a recent NIST compilation (*21*) using log-log interpolation. With Φ determined from Eq. (4), implementing a discrete form of Eq. (2) in the spreadsheet yielded absolute fluence spectra. Absolute spectra were corrected for air attenuation and inverse square law effects back to a traditional benchmark reporting distance of 1 m.

Recalling that air kerma values are based on known chamber calibration factors, the above procedure for calculating absolute spectra could be applied to the NIST beam code spectra. To determine the absolute fluence spectrum for an unfiltered beam, an exponential filtering term is introduced to Eq. (4) and the discrete normalized fluence spectrum term $N_i(e)$ that represented the NIST beam code is replaced with $Nu_i(e)$ to represent the normalized unfiltered fluence spectrum:

$$X = \sum_{i=0}^{E/\Delta e} \Phi_u \cdot \left[\frac{\mu_{en}(e)}{\rho}\right]_{\text{air}} \cdot e \cdot Nu_i(e) \cdot \exp\left[-\rho\left(\frac{\mu}{\rho}\right)t\right] \cdot \Delta e. \quad (5)$$

In Eq. (5), X is still the known air kerma value for the filtered NIST beam code, t is the NIST beam code filter thickness, ρ is the filter density, (μ/ρ) in the exponent is the mass attenuation coefficient, and Φ_u is the total X-ray fluence for the unfiltered beam. The attenuation coefficients were interpolated from the NIST compilation (*21*) in the same fashion as the mass-energy absorption coefficients. Substituting Φ_u for Φ in Eq. (2) gives the absolute unfiltered spectra for any beam operating at a tube potential corresponding to E. Using the NIST mass attenuation coefficients, absolute fluence spectra can be calculated with an accuracy of better than 2% for any filtered beam by simple exponential attenuation of the absolute unfiltered fluence spectra.

VALIDATION OF SPECTRA

The robust technique described for calculating absolute spectra relies on accurate normalized fluence spectra. Therefore, the shape of the normalized spectrum must be validated. Proper unfolding of pulse-height distributions should cause the spectrum to maintain zero intensity up to the filtration cut-off energy. Improper detector response matrix weighting could cause a positive or negative plateau in the spectrum below the filtration cut-off energy. Straight-line, or nearly straight-line, shapes at the high-energy end of unfiltered and moderately filtered constant potential spectra are well supported by the theory of Kramers (*22*). Improper detector response matrix weighting, or an inaccurate photopeak efficiency curve, could cause concavity or bowing at the high-energy end of unfolded spectra.

A powerful and comprehensive method for validating the Monte Carlo detector response matrix and spectra unfolding technique was applied in this work.[2] The method requires verifying agreement between filtered spectra and attenuated unfiltered spectra for the same range of tube potentials. Although not necessary, the unfolding method is applied to a second detector and the unfolded spectra for that detector are compared for agreement with spectra from the primary detector acquired under identical conditions.

Figure 5 qualitatively indicates correct unfolding of the pulse-height distributions. The figure displays comparisons

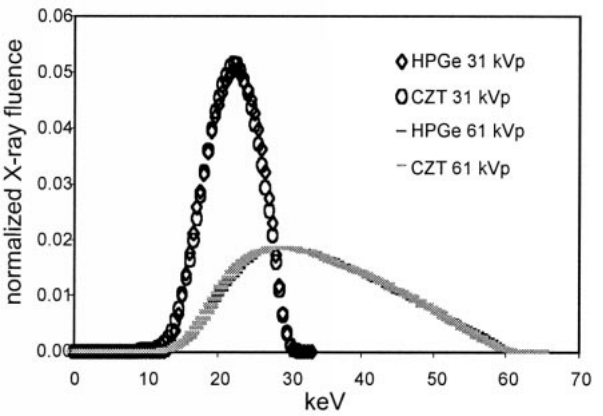

FIG. 6. Comparison of spectra measured with different spectroscopy detectors. Comparison of high-purity germanium and cadmium-zinc-telluride normalized X-ray fluence spectra for 1.528 mm aluminum added filtration at 31 and 61 kVp for the Seifert Isovolt system. Each spectrum was normalized to an area of 1.0 in fluence units of X rays/(mAs·cm²) at a 1-m distance from the tungsten anode target.

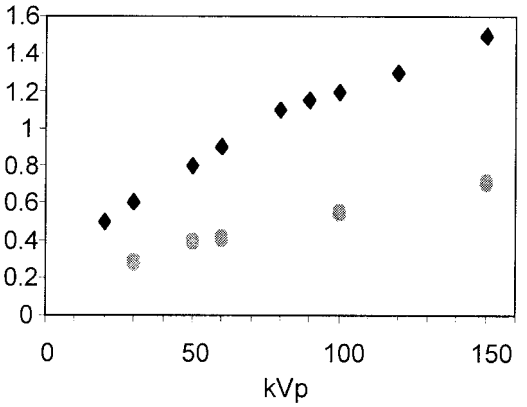

FIG. 7. Effective pitting and plating thickness as a function of kVp. Black diamonds (♦) indicate the energy dependence of effective pitting and plating thickness for 20° tungsten anode in the Seifert Isovolt system. For selected energies, gray dots (●) indicate the equivalent aluminum thickness when the beryllium window inherent tube filtration is added to the tungsten effective pitting and plating thickness. The ordinate has thickness units of μm of tungsten for black diamonds and mm of aluminum equivalence for gray dots.

between normalized filtered spectra with their companion spectra calculated by attenuating unfiltered spectra at 101.5 kVp. Note that spectra maintain zero intensity up to the filtration cut-off energies and that each moderately filtered spectrum displays a straight-line take-off at the maximum spectrum energy, in agreement with the theory of Kramers (*22*). The obvious agreement between a range-filtered spectrum and attenuated unfiltered spectra is a testament to the validity of the unfolding process and the accuracy and consistency of the manual peak stripping. The agreement is also a testament to the high accuracy of the NIST coefficients used in the attenuation calculations. The close agreement in the curves also confirms that the small amount of pulse pileup (<2%) in the unfiltered and lightly filtered beams proved insignificant in affecting spectral shapes. Although not shown, the same positive results were observed for various other filtrations at 31, 51, 61, 82, 93, 122 and 152 kVp.

The agreement in the companion spectra (Fig. 5) was quantified separately for continuum and K-shell peak portions of the curves. For the continuum portions, energy bins were excluded from the comparisons at the extremes of the continuum (e.g. values in the continuum below ~10% of the peak in the continuum) as were energy bins immediately surrounding the tungsten K-shell edge discontinuity in the continuum. The average agreement for any single 0.5-keV energy bin for all companion curve continua tended to be within 1–2%, with the highest single bin disagreement rarely exceeding 5% for 51 kVp and higher beams. The 31 kVp spectral errors were about double those of the other spectra due to less desirable counting statistics. Whereas most pulse-height distributions were acquired with about 1 million total counts, only about 250,000 total counts were acquired for the 31 kVp pulse-height distributions.

In evaluating K-shell peak intensities, a comparison of companion $K_{\alpha 1}$ peaks at 82, 93, 102, 122 and 152 kVp indicated typical agreement of 3–4% and was always better than 7%. Consistent and accurate peak stripping was further shown by a correct trend in the $K_{\beta 1}/K_{\alpha 1}$ ratio as a function of filtration and voltage.[2]

As stated previously, unfolding cadmium-zinc-telluride spectra was reliable for tube potentials up to ~70 kVp. In Fig. 6, a comparison for normalized unfolded high-purity germanium and cadmium-zinc-telluride spectra is shown at 31 and 61 kVp. The agreement in unfolded spectra between the two detectors is quite good. The level of agreement at 51 and 71 kVp paralleled that shown for 61 kVp in the figure. These results indicate that the overall spectral unfold-

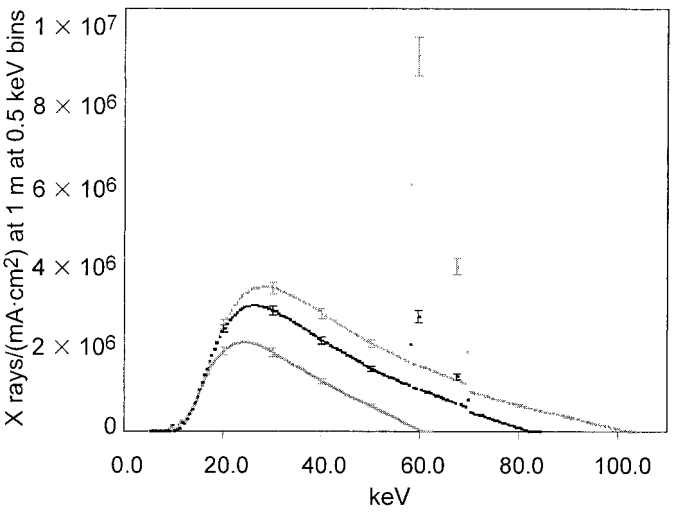

FIG. 8. Benchmark absolute fluence X-ray spectra for Seifert Isovolt system. Benchmark spectra from Seifert Isovolt system at 61.2, 82.4 and 101.5 kVp. Spectra have 7 mm beryllium inherent filtration, 0.5 mm aluminum added filtration, and effective pitting and plating thickness filtration from Fig. 7. Accuracy of the data is represented by error bars dispersed every ~10 keV and for $K_{\alpha 1}$ and $K_{\beta 1}$ peaks.

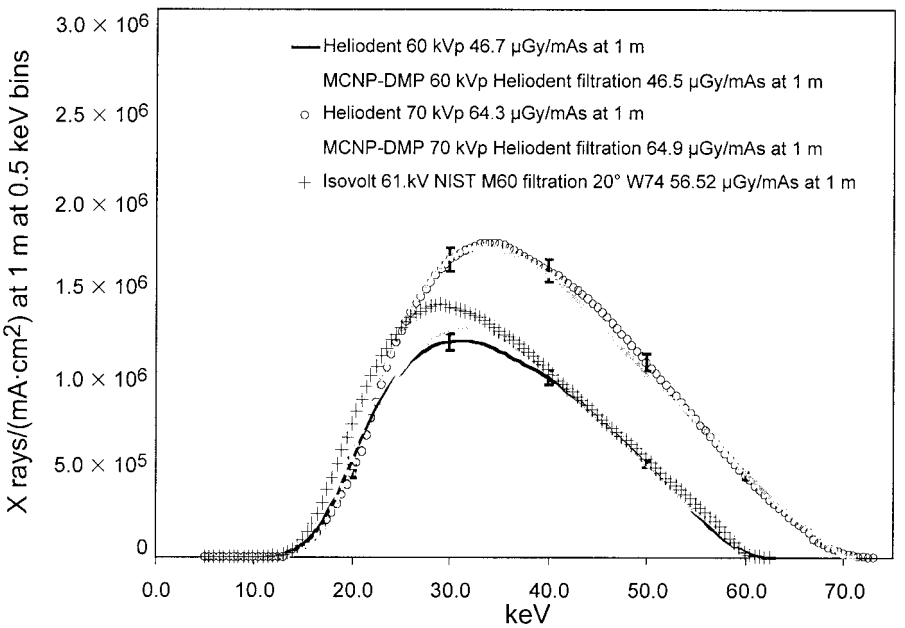

FIG. 9. Benchmark absolute fluence X-ray spectra for Siemens Heliodent system. Heliodent (pure tungsten target at 12° anode angle) benchmark spectra at 60 and 70 kVp with error bars every 10 keV. Isovolt NIST M60 beam is shown for qualitative comparison of spectrum shape and intensity. Monte Carlo-calculated spectra compare well with the Heliodent spectra measured with a cadmium-zinc-telluride detector.

ing process is sound. For smaller-sized detectors, Seltzer pointed out that the dominant correction in unfolding pulse-height distributions into correctly shaped spectra comes from the photopeak efficiency curve (*15*). This is the case for the cadmium-zinc-telluride crystal, which is only 2 mm thick. The cadmium-zinc-telluride photopeak efficiency curve imposes large corrections to the pulse-height distributions, whereas the high-purity germanium curve for a 5-cm-thick crystal is relatively flat and does not alter the pulse-height distributions dramatically (Fig. 3). At a minimum, the high level of agreement in the spectra in Fig. 6 validates the Monte Carlo-generated photopeak efficiency curves below 70 keV. Above 70 keV, Monte Carlo high-purity germanium photopeak efficiency curve follows the same trend line as the analytical version of the curve (Fig. 3).

ANODE PITTING AND DETECTOR DEAD LAYER

Pitting and cratering on the anode surface and plating out of vaporized anode material on the exit port window of the X-ray tube will decrease beam intensity and harden the spectrum. An assessment of the effective pitting and plating thickness is important for characterizing X-ray beams for benchmarking. This is particularly true for unfiltered and lightly filtered beams, where the effective pitting and plating thickness can have a dramatic effect on spectral shape. The values of effective pitting and plating thickness as a function of tube potential, along with the millimeters aluminum equivalence (mm Al_{eq}) of the total inherent filtration (e.g. 7 mm beryllium plus effective pitting and plating thickness), is plotted in Fig. 7 for the Isovolt X-ray tube. The effective pitting and plating thickness values in the plot were derived from differences in measured and Monte Carlo-calculated spectra.[2]

Figure 7 indicates that pitting is dominant over window plating for the fixed anode. The rise in effective pitting and plating thickness values with energy is consistent with pitting and not with plating or detector dead layer. Plating thickness would be constant regardless of tube potential, as would detector dead layer. Given the geometry of pitting and the increased range of electrons with kVp, greater effective pitting and plating thickness values are expected for higher-energy beams. By extrapolating the effective pitting and plating thickness data in Fig. 7 to 0 kVp, the maximum possible plating thickness, and/or equivalent detector dead layer, can be estimated as ~0.3 μm of tungsten ($Z = 74$). Interestingly, the 0 kVp extrapolated effective pitting and plating thickness value of 0.3 μm is roughly equivalent in low-energy X-ray attenuation performance to 3 μm of germanium (i.e. the listed high-purity germanium crystal dead-layer thickness).

ABSOLUTE SPECTRA: RESULTS

Benchmark spectra resulting from this work consist of well-characterized lightly filtered spectra from the Seifert Isovolt system and typically filtered dental spectra from the Heliodent unit. Lightly filtered spectra were chosen over unfiltered spectra to eliminate larger errors associated with energies below ~10 keV. Using NIST coefficients (*21*), the lightly filtered spectra can be attenuated to produce benchmark spectra of heavier filtrations only while adding about 1% to the total fluence error in the spectra. The benchmark spectra, with assigned errors, are tabulated in the Appendix.

Some of the tabulated benchmark spectra from the Seifert Isovolt system are shown graphically in Fig. 8.

Heliodent spectra are presented in Fig. 9 with Monte Carlo-calculated spectra. The Isovolt spectra were used to validate a modified version of the MCNP4B2 Monte Carlo code[2] (*16*). The code was then used to predict spectra from the Heliodent unit. Figure 9 shows good agreement for shape and intensity between measured and predicted Heliodent spectra. Unlike the Isovolt spectra, Heliodent pulse-height distributions were measured only with a cadmium-zinc-telluride detector and air kerma only with the MDH monitor. As a result of the measurement differences, the Heliodent spectra errors are larger than those of the Isovolt system. Since greater inherent filtration in the Heliodent unit removes more of the low-energy X rays than that in the Isovolt system, the effective pitting and plating thickness values were more difficult to assess. Whereas effective pitting and plating thickness errors for characterizing the Isovolt beams are about ± 0.1 μm, the errors for Heliodent beams are more like ± 0.5 μm.

CONCLUSIONS

The research of Fewell *et al.* (*5*), Hettinger and Starfelt (*6*), Israel *et al.* (*7*), Marshall *et al.* (*8*), Seelentag and Panzer (*10*), and Seltzer (*15*) provides a good foundation for the present work. Expanding on previous research, we have introduced and explained the requirements for benchmark spectra, weighting of the Monte Carlo detector response matrix, a method to assess anode pitting for beam characterization, quantitative laser and X-ray beam alignment, and a process for validating the spectral unfolding method. A primary goal of the research was to generate tungsten spectra in the diagnostic energy range that was well characterized for validation of a Monte Carlo code. This goal was achieved. The high level of detail and quality control in all phases of spectral measurements, unfolding, validation and characterization was successful in producing benchmark-quality absolute fluence spectra with known and reasonably small errors. Benchmark spectra, with errors, are tabulated in the Appendix for use by others.

APPENDIX

Benchmark Spectra for Primary X-Ray Beams[a]

Tube	Isovolt[b]	Isovolt[b]	Isovolt[b]	Isovolt[b]	Isovolt[b]
μGy/mAs at 1 m	336.4	264.3	215.1	206.2	177.5
EPPT ($\pm$ 0.1 μm)	1.4 μm	1.3 μm	1.2 μm	1.15 μm	1.1 μm
keV	151.8 kVp	122.3 kVp	101.5 kVp	92.8 kVp	82.4 kVp
5.0	*0.00*	*0.00*	*0.00*	*0.00*	*0.00*
5.5	*0.00*	*0.00*	*0.00*	*0.00*	*0.00*
6.0	*0.00*	*0.00*	*0.00*	*0.00*	*0.00*
6.5	*0.00*	*0.00*	*0.00*	*0.00*	*0.00*
7.0	*0.00*	*0.00*	*0.00*	*0.00*	*0.00*
7.5	*2.57×10^{1}*	*0.00*	*4.66×10^{1}*	*1.94×10^{2}*	*0.00*
8.0	*2.98×10^{2}*	*0.00*	*3.83×10^{2}*	*9.44×10^{2}*	*0.00*
8.5	*1.48×10^{3}*	*0.00*	*1.74×10^{3}*	*3.35×10^{3}*	*0.00*
9.0	*4.97×10^{3}*	*1.30×10^{3}*	*5.59×10^{3}*	*9.24×10^{3}*	*0.00*
9.5	*1.32×10^{5}*	*1.26×10^{5}*	*1.44×10^{5}*	*1.40×10^{5}*	*1.33×10^{5}*
10.0	*2.79×10^{4}*	*1.73×10^{4}*	*3.01×10^{4}*	*4.18×10^{4}*	*1.07×10^{4}*
10.5	*5.28×10^{4}*	*3.79×10^{4}*	*5.65×10^{4}*	*7.40×10^{4}*	*2.89×10^{4}*
11.0	*9.02×10^{4}*	*7.12×10^{4}*	*9.56×10^{4}*	*1.20×10^{5}*	*6.11×10^{4}*
11.5	*2.36×10^{5}*	*2.14×10^{5}*	*2.51×10^{5}*	*2.74×10^{5}*	*2.16×10^{5}*
12.0	*2.09×10^{5}*	*1.85×10^{5}*	*2.19×10^{5}*	*2.57×10^{5}*	*1.83×10^{5}*
12.5	*2.92×10^{5}*	*2.69×10^{5}*	*3.05×10^{5}*	*3.49×10^{5}*	*2.80×10^{5}*
13.0	*3.90×10^{5}*	*3.71×10^{5}*	*4.06×10^{5}*	*4.55×10^{5}*	*3.94×10^{5}*
13.5	*5.03×10^{5}*	*4.91×10^{5}*	*5.22×10^{5}*	*5.75×10^{5}*	*5.23×10^{5}*
14.0	*6.31×10^{5}*	*6.33×10^{5}*	*6.53×10^{5}*	7.08×10^{5}	6.65×10^{5}
14.5	*7.70×10^{5}*	*7.98×10^{5}*	*7.96×10^{5}*	8.51×10^{5}	8.18×10^{5}
15.0	*9.22×10^{5}*	9.84×10^{5}	9.50×10^{5}	1.00×10^{6}	9.80×10^{5}
15.5	1.08×10^{6}	1.16×10^{6}	1.11×10^{6}	1.16×10^{6}	1.15×10^{6}
16.0	1.31×10^{6}	1.33×10^{6}	1.29×10^{6}	1.34×10^{6}	1.32×10^{6}
16.5	1.52×10^{6}	1.52×10^{6}	1.46×10^{6}	1.51×10^{6}	1.49×10^{6}
17.0	1.72×10^{6}	1.71×10^{6}	1.64×10^{6}	1.69×10^{6}	1.66×10^{6}
17.5	1.92×10^{6}	1.90×10^{6}	1.81×10^{6}	1.87×10^{6}	1.81×10^{6}
18.0	2.12×10^{6}	2.09×10^{6}	1.97×10^{6}	2.03×10^{6}	1.95×10^{6}
18.5	2.32×10^{6}	2.26×10^{6}	2.13×10^{6}	2.18×10^{6}	2.09×10^{6}
19.0	2.51×10^{6}	2.44×10^{6}	2.28×10^{6}	2.33×10^{6}	2.22×10^{6}
19.5	2.70×10^{6}	2.60×10^{6}	2.41×10^{6}	2.47×10^{6}	2.34×10^{6}
20.0	2.87×10^{6}	2.75×10^{6}	2.54×10^{6}	2.59×10^{6}	2.44×10^{6}
20.5	3.05×10^{6}	2.90×10^{6}	2.66×10^{6}	2.71×10^{6}	2.54×10^{6}

APPENDIX

Continued[a]

Tube μGy/mAs at 1 m EPPT (± 0.1 μm) keV	Isovolt[b] 336.4 1.4 μm 151.8 kVp	Isovolt[b] 264.3 1.3 μm 122.3 kVp	Isovolt[b] 215.1 1.2 μm 101.5 kVp	Isovolt[b] 206.2 1.15 μm 92.8 kVp	Isovolt[b] 177.5 1.1 μm 82.4 kVp
21.0	3.21×10^6	3.04×10^6	2.78×10^6	2.81×10^6	2.64×10^6
21.5	3.37×10^6	3.17×10^6	2.88×10^6	2.91×10^6	2.70×10^6
22.0	3.52×10^6	3.29×10^6	2.97×10^6	3.00×10^6	2.76×10^6
22.5	3.66×10^6	3.40×10^6	3.05×10^6	3.06×10^6	2.82×10^6
23.0	3.79×10^6	3.50×10^6	3.13×10^6	3.13×10^6	2.86×10^6
23.5	3.91×10^6	3.60×10^6	3.19×10^6	3.19×10^6	2.89×10^6
24.0	4.02×10^6	3.67×10^6	3.24×10^6	3.23×10^6	2.92×10^6
24.5	4.13×10^6	3.75×10^6	3.28×10^6	3.26×10^6	2.94×10^6
25.0	4.22×10^6	3.81×10^6	3.32×10^6	3.28×10^6	2.97×10^6
25.5	4.30×10^6	3.87×10^6	3.35×10^6	3.31×10^6	2.98×10^6
26.0	4.38×10^6	3.91×10^6	3.38×10^6	3.33×10^6	2.98×10^6
26.5	4.45×10^6	3.94×10^6	3.39×10^6	3.34×10^6	2.97×10^6
27.0	4.50×10^6	3.97×10^6	3.40×10^6	3.34×10^6	2.96×10^6
27.5	4.55×10^6	3.99×10^6	3.42×10^6	3.34×10^6	2.95×10^6
28.0	4.59×10^6	4.01×10^6	3.42×10^6	3.33×10^6	2.94×10^6
28.5	4.64×10^6	4.02×10^6	3.42×10^6	3.33×10^6	2.92×10^6
29.0	4.67×10^6	4.03×10^6	3.41×10^6	3.30×10^6	2.91×10^6
29.5	4.70×10^6	4.03×10^6	3.41×10^6	3.29×10^6	2.88×10^6
30.0	4.71×10^6	4.02×10^6	3.40×10^6	3.27×10^6	2.85×10^6
30.5	4.73×10^6	4.02×10^6	3.38×10^6	3.24×10^6	2.83×10^6
31.0	4.74×10^6	4.00×10^6	3.35×10^6	3.22×10^6	2.79×10^6
31.5	4.75×10^6	3.99×10^6	3.33×10^6	3.19×10^6	2.76×10^6
32.0	4.75×10^6	3.98×10^6	3.30×10^6	3.16×10^6	2.74×10^6
32.5	4.75×10^6	3.97×10^6	3.28×10^6	3.13×10^6	2.70×10^6
33.0	4.75×10^6	3.95×10^6	3.25×10^6	3.10×10^6	2.67×10^6
33.5	4.74×10^6	3.91×10^6	3.22×10^6	3.07×10^6	2.63×10^6
34.0	4.71×10^6	3.88×10^6	3.20×10^6	3.03×10^6	2.59×10^6
34.5	4.69×10^6	3.85×10^6	3.17×10^6	2.99×10^6	2.55×10^6
35.0	4.66×10^6	3.82×10^6	3.14×10^6	2.96×10^6	2.53×10^6
35.5	4.64×10^6	3.78×10^6	3.10×10^6	2.92×10^6	2.48×10^6
36.0	4.61×10^6	3.75×10^6	3.07×10^6	2.88×10^6	2.45×10^6
36.5	4.59×10^6	3.73×10^6	3.04×10^6	2.84×10^6	2.42×10^6
37.0	4.56×10^6	3.69×10^6	3.01×10^6	2.81×10^6	2.38×10^6
37.5	4.54×10^6	3.66×10^6	2.98×10^6	2.77×10^6	2.33×10^6
38.0	4.50×10^6	3.62×10^6	2.94×10^6	2.73×10^6	2.29×10^6
38.5	4.46×10^6	3.59×10^6	2.91×10^6	2.69×10^6	2.25×10^6
39.0	4.44×10^6	3.56×10^6	2.87×10^6	2.65×10^6	2.21×10^6
39.5	4.41×10^6	3.53×10^6	2.83×10^6	2.62×10^6	2.17×10^6
40.0	4.38×10^6	3.49×10^6	2.79×10^6	2.58×10^6	2.14×10^6
40.5	4.34×10^6	3.44×10^6	2.75×10^6	2.55×10^6	2.11×10^6
41.0	4.30×10^6	3.41×10^6	2.71×10^6	2.50×10^6	2.07×10^6
41.5	4.28×10^6	3.37×10^6	2.67×10^6	2.46×10^6	2.04×10^6
42.0	4.24×10^6	3.33×10^6	2.63×10^6	2.43×10^6	2.00×10^6
42.5	4.20×10^6	3.30×10^6	2.60×10^6	2.39×10^6	1.97×10^6
43.0	4.16×10^6	3.27×10^6	2.56×10^6	2.35×10^6	1.93×10^6
43.5	4.13×10^6	3.22×10^6	2.53×10^6	2.31×10^6	1.90×10^6
44.0	4.09×10^6	3.18×10^6	2.49×10^6	2.27×10^6	1.87×10^6
44.5	4.06×10^6	3.14×10^6	2.45×10^6	2.23×10^6	1.84×10^6
45.0	4.02×10^6	3.10×10^6	2.42×10^6	2.20×10^6	1.81×10^6
45.5	3.99×10^6	3.07×10^6	2.38×10^6	2.16×10^6	1.77×10^6
46.0	3.96×10^6	3.04×10^6	2.35×10^6	2.13×10^6	1.74×10^6
46.5	3.92×10^6	3.01×10^6	2.32×10^6	2.10×10^6	1.71×10^6
47.0	3.88×10^6	2.98×10^6	2.28×10^6	2.07×10^6	1.67×10^6
47.5	3.84×10^6	2.94×10^6	2.25×10^6	2.04×10^6	1.64×10^6
48.0	3.80×10^6	2.90×10^6	2.22×10^6	2.01×10^6	1.61×10^6
48.5	3.77×10^6	2.86×10^6	2.19×10^6	1.97×10^6	1.57×10^6
49.0	3.73×10^6	2.83×10^6	2.15×10^6	1.94×10^6	1.53×10^6
49.5	3.70×10^6	2.80×10^6	2.12×10^6	1.90×10^6	1.50×10^6
50.0	3.66×10^6	2.77×10^6	2.09×10^6	1.87×10^6	1.47×10^6

APPENDIX

Continued[a]

Tube μGy/mAs at 1 m EPPT (± 0.1 μm) keV	Isovolt[b] 336.4 1.4 μm 151.8 kVp	Isovolt[b] 264.3 1.3 μm 122.3 kVp	Isovolt[b] 215.1 1.2 μm 101.5 kVp	Isovolt[b] 206.2 1.15 μm 92.8 kVp	Isovolt[b] 177.5 1.1 μm 82.4 kVp
50.5	3.62×10^{6}	2.74×10^{6}	2.06×10^{6}	1.84×10^{6}	1.44×10^{6}
51.0	3.58×10^{6}	2.71×10^{6}	2.03×10^{6}	1.81×10^{6}	1.42×10^{6}
51.5	3.56×10^{6}	2.68×10^{6}	2.00×10^{6}	1.77×10^{6}	1.39×10^{6}
52.0	3.52×10^{6}	2.64×10^{6}	1.97×10^{6}	1.73×10^{6}	1.37×10^{6}
52.5	3.49×10^{6}	2.62×10^{6}	1.94×10^{6}	1.70×10^{6}	1.34×10^{6}
53.0	3.46×10^{6}	2.59×10^{6}	1.91×10^{6}	1.67×10^{6}	1.31×10^{6}
53.5	3.44×10^{6}	2.56×10^{6}	1.88×10^{6}	1.64×10^{6}	1.28×10^{6}
54.0	3.40×10^{6}	2.53×10^{6}	1.85×10^{6}	1.61×10^{6}	1.26×10^{6}
54.5	3.37×10^{6}	2.50×10^{6}	1.82×10^{6}	1.58×10^{6}	1.23×10^{6}
55.0	3.34×10^{6}	2.47×10^{6}	1.79×10^{6}	1.55×10^{6}	1.21×10^{6}
55.5	3.30×10^{6}	2.44×10^{6}	1.76×10^{6}	1.52×10^{6}	1.18×10^{6}
56.0	3.27×10^{6}	2.41×10^{6}	1.74×10^{6}	1.50×10^{6}	1.16×10^{6}
56.5	3.24×10^{6}	2.37×10^{6}	1.71×10^{6}	1.47×10^{6}	1.14×10^{6}
57.0	3.20×10^{6}	2.34×10^{6}	1.68×10^{6}	1.45×10^{6}	1.12×10^{6}
57.5	$\mathbf{3.17 \times 10^{6}}$	$\mathbf{2.31 \times 10^{6}}$	$\mathbf{1.66 \times 10^{6}}$	$\mathbf{1.42 \times 10^{6}}$	$\mathbf{1.09 \times 10^{6}}$
58.0	$\mathbf{2.01 \times 10^{7}}$	$\mathbf{1.11 \times 10^{7}}$	$\mathbf{5.85 \times 10^{6}}$	$\mathbf{4.02 \times 10^{6}}$	*2.06 × 10⁶*
58.5	$\mathbf{3.10 \times 10^{6}}$	$\mathbf{2.25 \times 10^{6}}$	$\mathbf{1.60 \times 10^{6}}$	$\mathbf{1.38 \times 10^{6}}$	$\mathbf{1.05 \times 10^{6}}$
59.0	$\mathbf{3.07 \times 10^{6}}$	$\mathbf{2.22 \times 10^{6}}$	$\mathbf{1.58 \times 10^{6}}$	$\mathbf{1.35 \times 10^{6}}$	$\mathbf{1.03 \times 10^{6}}$
59.5	$\mathbf{3.26 \times 10^{7}}$	$\mathbf{1.75 \times 10^{7}}$	$\mathbf{8.89 \times 10^{6}}$	$\mathbf{5.88 \times 10^{6}}$	*2.73 × 10⁶*
60.0	$\mathbf{3.01 \times 10^{6}}$	$\mathbf{2.17 \times 10^{6}}$	$\mathbf{1.54 \times 10^{6}}$	$\mathbf{1.31 \times 10^{6}}$	$\mathbf{9.85 \times 10^{5}}$
60.5	$\mathbf{2.97 \times 10^{6}}$	$\mathbf{2.14 \times 10^{6}}$	$\mathbf{1.52 \times 10^{6}}$	$\mathbf{1.29 \times 10^{6}}$	$\mathbf{9.63 \times 10^{5}}$
61.0	$\mathbf{2.94 \times 10^{6}}$	$\mathbf{2.11 \times 10^{6}}$	$\mathbf{1.50 \times 10^{6}}$	$\mathbf{1.26 \times 10^{6}}$	$\mathbf{9.41 \times 10^{5}}$
61.5	$\mathbf{2.91 \times 10^{6}}$	$\mathbf{2.08 \times 10^{6}}$	$\mathbf{1.47 \times 10^{6}}$	$\mathbf{1.24 \times 10^{6}}$	$\mathbf{9.19 \times 10^{5}}$
62.0	$\mathbf{2.88 \times 10^{6}}$	$\mathbf{2.06 \times 10^{6}}$	$\mathbf{1.45 \times 10^{6}}$	$\mathbf{1.22 \times 10^{6}}$	$\mathbf{8.97 \times 10^{5}}$
62.5	$\mathbf{2.85 \times 10^{6}}$	$\mathbf{2.03 \times 10^{6}}$	$\mathbf{1.43 \times 10^{6}}$	$\mathbf{1.20 \times 10^{6}}$	$\mathbf{8.75 \times 10^{5}}$
63.0	$\mathbf{2.81 \times 10^{6}}$	$\mathbf{2.00 \times 10^{6}}$	$\mathbf{1.41 \times 10^{6}}$	$\mathbf{1.18 \times 10^{6}}$	$\mathbf{8.53 \times 10^{5}}$
63.5	$\mathbf{2.78 \times 10^{6}}$	$\mathbf{1.97 \times 10^{6}}$	$\mathbf{1.39 \times 10^{6}}$	$\mathbf{1.16 \times 10^{6}}$	$\mathbf{8.31 \times 10^{5}}$
64.0	$\mathbf{2.75 \times 10^{6}}$	$\mathbf{1.94 \times 10^{6}}$	$\mathbf{1.36 \times 10^{6}}$	$\mathbf{1.14 \times 10^{6}}$	$\mathbf{8.09 \times 10^{5}}$
64.5	$\mathbf{2.72 \times 10^{6}}$	$\mathbf{1.92 \times 10^{6}}$	$\mathbf{1.34 \times 10^{6}}$	$\mathbf{1.12 \times 10^{6}}$	$\mathbf{7.87 \times 10^{5}}$
65.0	$\mathbf{2.68 \times 10^{6}}$	$\mathbf{1.89 \times 10^{6}}$	$\mathbf{1.32 \times 10^{6}}$	$\mathbf{1.10 \times 10^{6}}$	$\mathbf{7.65 \times 10^{5}}$
65.5	$\mathbf{2.65 \times 10^{6}}$	$\mathbf{1.86 \times 10^{6}}$	$\mathbf{1.30 \times 10^{6}}$	$\mathbf{1.08 \times 10^{6}}$	$\mathbf{7.43 \times 10^{5}}$
66.0	$\mathbf{2.62 \times 10^{6}}$	$\mathbf{1.83 \times 10^{6}}$	$\mathbf{1.28 \times 10^{6}}$	$\mathbf{1.06 \times 10^{6}}$	$\mathbf{7.21 \times 10^{5}}$
66.5	$\mathbf{2.59 \times 10^{6}}$	$\mathbf{1.80 \times 10^{6}}$	$\mathbf{1.25 \times 10^{6}}$	$\mathbf{1.04 \times 10^{6}}$	$\mathbf{6.99 \times 10^{5}}$
67.0	$\mathbf{2.55 \times 10^{6}}$	$\mathbf{1.77 \times 10^{6}}$	$\mathbf{1.23 \times 10^{6}}$	$\mathbf{1.02 \times 10^{6}}$	$\mathbf{6.77 \times 10^{5}}$
67.5	$\mathbf{1.30 \times 10^{6}}$	$\mathbf{7.33 \times 10^{6}}$	$\mathbf{3.90 \times 10^{6}}$	$\mathbf{2.68 \times 10^{6}}$	*1.29 × 10⁶*
68.0	$\mathbf{2.49 \times 10^{6}}$	$\mathbf{1.72 \times 10^{6}}$	$\mathbf{1.19 \times 10^{6}}$	$\mathbf{9.83 \times 10^{5}}$	$\mathbf{6.33 \times 10^{5}}$
68.5	$\mathbf{2.46 \times 10^{6}}$	$\mathbf{1.69 \times 10^{6}}$	$\mathbf{1.16 \times 10^{6}}$	$\mathbf{9.63 \times 10^{5}}$	$\mathbf{6.11 \times 10^{5}}$
69.0	$\mathbf{2.42 \times 10^{6}}$	$\mathbf{1.66 \times 10^{6}}$	$\mathbf{1.14 \times 10^{6}}$	$\mathbf{9.44 \times 10^{5}}$	$\mathbf{5.89 \times 10^{5}}$
69.5	$\mathbf{5.34 \times 10^{6}}$	$\mathbf{3.21 \times 10^{6}}$	$\mathbf{1.88 \times 10^{6}}$	$\mathbf{1.40 \times 10^{6}}$	*7.48 × 10⁵*
70.0	$\mathbf{2.10 \times 10^{6}}$	$\mathbf{1.47 \times 10^{6}}$	$\mathbf{9.41 \times 10^{5}}$	$\mathbf{8.14 \times 10^{5}}$	$\mathbf{4.58 \times 10^{5}}$
70.5	$\mathbf{2.07 \times 10^{6}}$	$\mathbf{1.45 \times 10^{6}}$	$\mathbf{9.24 \times 10^{5}}$	$\mathbf{7.96 \times 10^{5}}$	$\mathbf{4.39 \times 10^{5}}$
71.0	$\mathbf{2.05 \times 10^{6}}$	$\mathbf{1.43 \times 10^{6}}$	$\mathbf{9.08 \times 10^{5}}$	$\mathbf{7.77 \times 10^{5}}$	$\mathbf{4.20 \times 10^{5}}$
71.5	$\mathbf{2.03 \times 10^{6}}$	$\mathbf{1.41 \times 10^{6}}$	$\mathbf{8.92 \times 10^{5}}$	$\mathbf{7.59 \times 10^{5}}$	$\mathbf{4.01 \times 10^{5}}$
72.0	$\mathbf{2.00 \times 10^{6}}$	$\mathbf{1.39 \times 10^{6}}$	$\mathbf{8.76 \times 10^{5}}$	$\mathbf{7.41 \times 10^{5}}$	$\mathbf{3.82 \times 10^{5}}$
72.5	$\mathbf{1.98 \times 10^{6}}$	$\mathbf{1.37 \times 10^{6}}$	$\mathbf{8.59 \times 10^{5}}$	$\mathbf{7.22 \times 10^{5}}$	$\mathbf{3.63 \times 10^{5}}$
73.0	$\mathbf{1.95 \times 10^{6}}$	$\mathbf{1.35 \times 10^{6}}$	$\mathbf{8.43 \times 10^{5}}$	$\mathbf{7.04 \times 10^{5}}$	$\mathbf{3.44 \times 10^{5}}$
73.5	$\mathbf{1.93 \times 10^{6}}$	$\mathbf{1.33 \times 10^{6}}$	$\mathbf{8.27 \times 10^{5}}$	$\mathbf{6.85 \times 10^{5}}$	$\mathbf{3.25 \times 10^{5}}$
74.0	$\mathbf{1.91 \times 10^{6}}$	$\mathbf{1.31 \times 10^{6}}$	$\mathbf{8.10 \times 10^{5}}$	$\mathbf{6.67 \times 10^{5}}$	$\mathbf{3.06 \times 10^{5}}$
74.5	$\mathbf{1.88 \times 10^{6}}$	$\mathbf{1.30 \times 10^{6}}$	$\mathbf{7.94 \times 10^{5}}$	$\mathbf{6.49 \times 10^{5}}$	$\mathbf{2.87 \times 10^{5}}$
75.0	$\mathbf{1.86 \times 10^{6}}$	$\mathbf{1.28 \times 10^{6}}$	$\mathbf{7.78 \times 10^{5}}$	$\mathbf{6.30 \times 10^{5}}$	$\mathbf{2.68 \times 10^{5}}$
75.5	$\mathbf{1.84 \times 10^{6}}$	$\mathbf{1.26 \times 10^{6}}$	$\mathbf{7.62 \times 10^{5}}$	$\mathbf{6.12 \times 10^{5}}$	$\mathbf{2.49 \times 10^{5}}$
76.0	$\mathbf{1.81 \times 10^{6}}$	$\mathbf{1.24 \times 10^{6}}$	$\mathbf{7.45 \times 10^{5}}$	$\mathbf{5.93 \times 10^{5}}$	$\mathbf{2.31 \times 10^{5}}$
76.5	$\mathbf{1.79 \times 10^{6}}$	$\mathbf{1.22 \times 10^{6}}$	$\mathbf{7.29 \times 10^{5}}$	$\mathbf{5.75 \times 10^{5}}$	$\mathbf{2.12 \times 10^{5}}$
77.0	$\mathbf{1.77 \times 10^{6}}$	$\mathbf{1.20 \times 10^{6}}$	$\mathbf{7.13 \times 10^{5}}$	$\mathbf{5.57 \times 10^{5}}$	$\mathbf{1.93 \times 10^{5}}$
77.5	$\mathbf{1.74 \times 10^{6}}$	$\mathbf{1.18 \times 10^{6}}$	$\mathbf{6.96 \times 10^{5}}$	$\mathbf{5.38 \times 10^{5}}$	$\mathbf{1.74 \times 10^{5}}$
78.0	$\mathbf{1.72 \times 10^{6}}$	$\mathbf{1.16 \times 10^{6}}$	$\mathbf{6.80 \times 10^{5}}$	$\mathbf{5.20 \times 10^{5}}$	*1.55 × 10⁵*
78.5	$\mathbf{1.70 \times 10^{6}}$	$\mathbf{1.14 \times 10^{6}}$	$\mathbf{6.64 \times 10^{5}}$	$\mathbf{5.02 \times 10^{5}}$	*1.36 × 10⁵*
79.0	$\mathbf{1.67 \times 10^{6}}$	$\mathbf{1.12 \times 10^{6}}$	$\mathbf{6.46 \times 10^{5}}$	$\mathbf{4.84 \times 10^{5}}$	*1.17 × 10⁵*
79.5	$\mathbf{1.65 \times 10^{6}}$	$\mathbf{1.10 \times 10^{6}}$	$\mathbf{6.30 \times 10^{5}}$	$\mathbf{4.65 \times 10^{5}}$	*9.77 × 10⁴*

APPENDIX

Continued[a]

Tube μGy/mAs at 1 m EPPT (± 0.1 μm) keV	Isovolt[b] 336.4 1.4 μm 151.8 kVp	Isovolt[b] 264.3 1.3 μm 122.3 kVp	Isovolt[b] 215.1 1.2 μm 101.5 kVp	Isovolt[b] 206.2 1.15 μm 92.8 kVp	Isovolt[b] 177.5 1.1 μm 82.4 kVp
80.0	**1.62 × 10⁶**	**1.08 × 10⁶**	**6.14 × 10⁵**	**4.47 × 10⁵**	*7.88 × 10⁴*
80.5	1.60 × 10⁶	1.06 × 10⁶	5.97 × 10⁵	4.29 × 10⁵	*5.98 × 10⁴*
81.0	1.58 × 10⁶	1.04 × 10⁶	5.81 × 10⁵	4.11 × 10⁵	*4.08 × 10⁴*
81.5	1.56 × 10⁶	1.03 × 10⁶	5.66 × 10⁵	3.95 × 10⁵	*2.51 × 10⁴*
82.0	1.54 × 10⁶	1.01 × 10⁶	5.51 × 10⁵	3.77 × 10⁵	*1.31 × 10⁴*
82.5	1.52 × 10⁶	9.89 × 10⁵	5.36 × 10⁵	3.61 × 10⁵	*4.94 × 10³*
83.0	1.51 × 10⁶	9.71 × 10⁵	5.25 × 10⁵	3.42 × 10⁵	*0.00*
83.5	1.49 × 10⁶	9.54 × 10⁵	5.12 × 10⁵	3.25 × 10⁵	*0.00*
84.0	1.47 × 10⁶	9.33 × 10⁵	4.99 × 10⁵	3.07 × 10⁵	
84.5	1.45 × 10⁶	9.16 × 10⁵	4.88 × 10⁵	2.89 × 10⁵	
85.0	1.43 × 10⁶	9.02 × 10⁵	4.75 × 10⁵	2.72 × 10⁵	
85.5	1.41 × 10⁶	8.86 × 10⁵	4.61 × 10⁵	2.56 × 10⁵	
86.0	1.39 × 10⁶	8.70 × 10⁵	4.48 × 10⁵	2.38 × 10⁵	
86.5	1.37 × 10⁶	8.54 × 10⁵	4.36 × 10⁵	2.22 × 10⁵	
87.0	1.36 × 10⁶	8.36 × 10⁵	4.21 × 10⁵	2.03 × 10⁵	
87.5	1.34 × 10⁶	8.21 × 10⁵	4.08 × 10⁵	1.86 × 10⁵	
88.0	1.32 × 10⁶	8.07 × 10⁵	3.93 × 10⁵	*1.68 × 10⁵*	
88.5	1.30 × 10⁶	7.95 × 10⁵	3.77 × 10⁵	*1.52 × 10⁵*	
89.0	1.28 × 10⁶	7.79 × 10⁵	3.64 × 10⁵	*1.35 × 10⁵*	
89.5	1.27 × 10⁶	7.68 × 10⁵	3.48 × 10⁵	*1.18 × 10⁵*	
90.0	1.26 × 10⁶	7.57 × 10⁵	3.34 × 10⁵	*1.01 × 10⁵*	
90.5	1.25 × 10⁶	7.43 × 10⁵	3.20 × 10⁵	*8.40 × 10⁴*	
91.0	1.23 × 10⁶	7.26 × 10⁵	3.07 × 10⁵	*6.77 × 10⁴*	
91.5	1.22 × 10⁶	7.13 × 10⁵	2.94 × 10⁵	*5.41 × 10⁴*	
92.0	1.20 × 10⁶	6.97 × 10⁵	2.79 × 10⁵	*4.14 × 10⁴*	
92.5	1.18 × 10⁶	6.82 × 10⁵	2.66 × 10⁵	*1.65 × 10⁴*	
93.0	1.17 × 10⁶	6.70 × 10⁵	2.52 × 10⁵	*8.62 × 10³*	
93.5	1.16 × 10⁶	6.59 × 10⁵	2.40 × 10⁵	*0.00*	
94.0	1.14 × 10⁶	6.43 × 10⁵	2.26 × 10⁵		
94.5	1.13 × 10⁶	6.32 × 10⁵	2.12 × 10⁵		
95.0	1.12 × 10⁶	6.19 × 10⁵	*1.99 × 10⁵*		
95.5	1.11 × 10⁶	6.06 × 10⁵	*1.84 × 10⁵*		
96.0	1.09 × 10⁶	5.95 × 10	*1.69 × 10⁵*		
96.5	1.08 × 10⁶	5.83 × 10⁵	*1.56 × 10⁵*		
97.0	1.06 × 10⁶	5.69 × 10⁵	*1.41 × 10⁵*		
97.5	1.05 × 10⁶	5.61 × 10⁵	*1.27 × 10⁵*		
98.0	1.04 × 10⁶	5.53 × 10⁵	*1.14 × 10⁵*		
98.5	1.03 × 10⁶	5.40 × 10⁵	*9.90 × 10⁴*		
99.0	1.02 × 10⁶	5.27 × 10⁵	*8.47 × 10⁴*		
99.5	1.00 × 10⁶	5.18 × 10⁵	*6.94 × 10⁴*		
100.0	9.93 × 10⁵	5.05 × 10⁵	*5.44 × 10⁴*		
100.5	9.78 × 10⁵	4.93 × 10⁵	*4.01 × 10⁴*		
101.0	9.65 × 10⁵	4.82 × 10⁵	*2.81 × 10⁴*		
101.5	9.54 × 10⁵	4.70 × 10⁵	*1.80 × 10⁴*		
102.0	9.40 × 10⁵	4.59 × 10⁵	*1.05 × 10⁴*		
102.5	9.36 × 10⁵	4.52 × 10⁵	*5.99 × 10³*		
103.0	9.26 × 10⁵	4.37 × 10⁵	*2.90 × 10³*		
103.5	9.17 × 10⁵	4.24 × 10⁵	*0.00*		
104.0	9.05 × 10⁵	4.13 × 10⁵	*0.00*		
104.5	8.95 × 10⁵	4.02 × 10⁵			
105.0	8.84 × 10⁵	3.91 × 10⁵			
105.5	8.75 × 10⁵	3.79 × 10⁵			
106	8.64 × 10⁵	3.70 × 10⁵			
106.5	8.52 × 10⁵	3.58 × 10⁵			
107	8.41 × 10⁵	3.46 × 10⁵			
107.5	8.30 × 10⁵	3.37 × 10⁵			
108	8.20 × 10⁵	3.24 × 10⁵			
108.5	8.11 × 10⁵	3.14 × 10⁵			
109	8.01 × 10⁵	3.02 × 10⁵			

APPENDIX

Continued[a]

Tube μGy/mAs at 1 m EPPT (± 0.1 μm) keV	Isovolt[b] 336.4 1.4 μm 151.8 kVp	Isovolt[b] 264.3 1.3 μm 122.3 kVp	Isovolt[b] 215.1 1.2 μm 101.5 kVp	Isovolt[b] 206.2 1.15 μm 92.8 kVp	Isovolt[b] 177.5 1.1 μm 82.4 kVp
109.5	7.89×10^5	2.90×10^5			
110	7.81×10^5	2.80×10^5			
110.5	7.68×10^5	2.68×10^5			
111	7.57×10^5	2.58×10^5			
111.5	7.45×10^5	2.47×10^5			
112	7.36×10^5	2.35×10^5			
112.5	7.26×10^5	2.22×10^5			
113	7.18×10^5	2.09×10^5			
113.5	7.07×10^5	1.98×10^5			
114	6.91×10^5	1.87×10^5			
114.5	6.79×10^5	1.75×10^5			
115	6.67×10^5	*1.64 × 10⁵*			
115.5	6.56×10^5	*1.50 × 10⁵*			
116	6.48×10^5	*1.38 × 10⁵*			
116.5	6.35×10^5	*1.25 × 10⁵*			
117	6.27×10^5	*1.12 × 10⁵*			
117.5	6.18×10^5	*9.95 × 10⁴*			
118	6.10×10^5	*8.77 × 10⁴*			
118.5	5.99×10^5	*7.61 × 10⁴*			
119	5.88×10^5	*6.40 × 10⁴*			
119.5	5.80×10^5	*5.32 × 10⁴*			
120	5.73×10^5	*3.76 × 10⁴*			
120.5	5.66×10^5	*2.83 × 10⁴*			
121	5.56×10^5	*1.93 × 10⁴*			
121.5	5.46×10^5	*1.42 × 10⁴*			
122	5.40×10^5	*9.12 × 10³*			
122.5	5.33×10^5	*5.63 × 10³*			
123	5.25×10^5	*0.00*			
123.5	5.14×10^5	*0.00*			
124	5.03×10^5				
124.5	4.93×10^5				
125	4.87×10^5				
125.5	4.76×10^5				
126	4.68×10^5				
126.5	4.58×10^5				
127	4.52×10^5				
127.5	4.45×10^5				
128	4.34×10^5				
128.5	4.24×10^5				
129	4.14×10^5				
129.5	4.06×10^5				
130	4.00×10^5				
130.5	3.91×10^5				
131	3.82×10^5				
131.5	3.74×10^5				
132	3.68×10^5				
132.5	3.59×10^5				
133	3.46×10^5				
133.5	3.37×10^5				
134	3.29×10^5				
134.5	3.24×10^5				
135	3.19×10^5				
135.5	3.11×10^5				
136	2.99×10^5				
136.5	2.91×10^5				
137	2.82×10^5				
137.5	2.72×10^5				
138	2.59×10^5				
138.5	2.52×10^5				

APPENDIX

Continued[a]

Tube	Isovolt[b]	Isovolt[b]	Isovolt[b]	Isovolt[b]	Isovolt[b]
μGy/mAs at 1 m	336.4	264.3	215.1	206.2	177.5
EPPT (± 0.1 μm)	1.4 μm	1.3 μm	1.2 μm	1.15 μm	1.1 μm
keV	151.8 kVp	122.3 kVp	101.5 kVp	92.8 kVp	82.4 kVp
139	2.43×10^5				
139.5	2.31×10^5				
140	*2.20×10^5*				
140.5	*2.08×10^5*				
141	*1.99×10^5*				
141.5	*1.93×10^5*				
142	*1.82×10^5*				
142.5	*1.72×10^5*				
143	*1.62×10^5*				
143.5	*1.55×10^5*				
144	*1.45×10^5*				
144.5	*1.35×10^5*				
145	*1.25×10^5*				
145.5	*1.14×10^5*				
146	*1.03×10^5*				
146.5	*9.13×10^4*				
147	*7.95×10^4*				
147.5	*6.84×10^4*				
148	*5.46×10^4*				
148.5	*4.51×10^4*				
149	*3.47×10^4*				
149.5	*2.30×10^4*				
150	*1.61×10^4*				
150.5	*1.11×10^4*				
151	*6.02×10^4*				
151.5	*4.15×10^4*				
152.0	*3.01×10^3*				
152.5	*0.00*				
153.0	*0.00*				

Tube	Heliodent[c]	Isovolt[b]	Heliodent[c]	Isovolt[b]	Isovolt[b]
μGy/mAs at 1 m	64.3	121.1	46.7	88	3
EPPT (± 0.1 μm)	1 ± 0.5 μm	0.9 μm	1 ± 0.5 μm	0.8 μm	0.6 μm
keV	70 kVp	61.2 kVp	60 kVp	50.8 kVp	30.8 kVp
5.0	*0.00*	*0.00*	*0.00*	*0.00*	*0.00*
5.5	*0.00*	*0.00*	*0.00*	*0.00*	*0.00*
6.0	*0.00*	*0.00*	*0.00*	*0.00*	*0.00*
6.5	*0.00*	*0.00*	*0.00*	*0.00*	*6.26*
7.0	*0.00*	*0.00*	*0.00*	*0.00*	*5.78×10^1*
7.5	*0.00*	*2.72×10^1*	*0.00*	*0.00*	*3.13×10^2*
8.0	*0.00*	*2.90×10^2*	*0.00*	*0.00*	*1.17×10^3*
8.5	*0.00*	*1.42×10^3*	*0.00*	*1.25×10^2*	*3.37×10^3*
9.0	*0.00*	*4.70×10^3*	*0.00*	*1.52×10^3*	*7.91×10^3*
9.5	*0.00*	*1.38×10^5*	*0.00*	*6.73×10^4*	*6.62×10^4*
10.0	*0.00*	*2.62×10^4*	*0.00*	*1.42×10^4*	*2.82×10^4*
10.5	*0.00*	*4.95×10^4*	*0.00*	*2.98×10^4*	*4.60×10^4*
11.0	*0.00*	*8.44×10^4*	*0.00*	*5.46×10^4*	*6.96×10^4*
11.5	*0.00*	*2.48×10^5*	*0.00*	*1.39×10^5*	*1.42×10^5*
12.0	*0.00*	*1.95×10^5*	*1.65×10^3*	*1.38×10^5*	*1.34×10^5*
12.5	*0.00*	*2.72×10^5*	*5.09×10^3*	*1.98×10^5*	*1.74×10^5*
13.0	*0.00*	*3.64×10^5*	*1.06×10^4*	*2.72×10^5*	*2.19×10^5*
13.5	*9.38×10^3*	*4.69×10^5*	*1.93×10^4*	*3.58×10^5*	*2.69×10^5*
14.0	*2.14×10^4*	5.88×10^5	*3.21×10^4*	4.56×10^5	**3.22×10^5**
14.5	*3.64×10^4*	7.20×10^5	*4.77×10^4*	5.64×10^5	**3.76×10^5**
15.0	*5.51×10^4*	8.58×10^5	*6.65×10^4*	6.83×10^5	**4.27×10^5**
15.5	*7.98×10^4*	1.01×10^6	*9.02×10^4*	8.10×10^5	**4.76×10^5**
16.0	*1.03×10^5*	1.14×10^6	*1.18×10^5*	9.21×10^5	**5.19×10^5**
16.5	*1.31×10^5*	1.27×10^6	*1.51×10^5*	1.03×10^6	**5.52×10^5**
17.0	*1.64×10^5*	1.39×10^6	*1.89×10^5*	1.13×10^6	**5.77×10^5**

APPENDIX

Continued[a]

Tube	Heliodent[c]	Isovolt[b]	Heliodent[c]	Isovolt[b]	Isovolt[b]
μGy/mAs at 1 m	64.3	121.1	46.7	88	3
EPPT (± 0.1 μm)	1 ± 0.5 μm	0.9 μm	1 ± 0.5 μm	0.8 μm	0.6 μm
keV	70 kVp	61.2 kVp	60 kVp	50.8 kVp	30.8 kVp
17.5	2.02×10^5	1.50×10^6	2.34×10^5	1.22×10^6	$\mathbf{5.99 \times 10^5}$
18.0	2.44×10^5	1.60×10^6	2.84×10^5	1.30×10^6	$\mathbf{6.13 \times 10^5}$
18.5	2.91×10^5	1.69×10^6	3.39×10^5	1.36×10^6	$\mathbf{6.24 \times 10^5}$
19.0	3.42×10^5	1.76×10^6	3.98×10^5	1.42×10^6	$\mathbf{6.29 \times 10^5}$
19.5	3.96×10^5	1.83×10^6	4.61×10^5	1.48×10^6	$\mathbf{6.32 \times 10^5}$
20.0	4.54×10^5	1.89×10^6	5.22×10^5	1.52×10^6	$\mathbf{6.30 \times 10^5}$
20.5	5.16×10^5	1.94×10^6	5.85×10^5	1.55×10^6	$\mathbf{6.29 \times 10^5}$
21.0	5.80×10^5	1.98×10^6	6.47×10^5	1.59×10^6	$\mathbf{6.23 \times 10^5}$
21.5	6.68×10^5	2.03×10^6	7.07×10^5	1.62×10^6	$\mathbf{6.14 \times 10^5}$
22.0	7.58×10^5	2.06×10^6	7.62×10^5	1.63×10^6	$\mathbf{6.00 \times 10^5}$
22.5	8.49×10^5	2.08×10^6	8.15×10^5	1.65×10^6	$\mathbf{5.79 \times 10^5}$
23.0	9.41×10^5	2.10×10^6	8.63×10^5	1.65×10^6	$\mathbf{5.57 \times 10^5}$
23.5	1.03×10^6	2.11×10^6	9.06×10^5	1.65×10^6	$\mathbf{5.31 \times 10^5}$
24.0	1.10×10^6	2.11×10^6	9.44×10^5	1.64×10^6	$\mathbf{5.03 \times 10^5}$
24.5	1.17×10^6	2.10×10^6	9.79×10^5	1.63×10^6	$\mathbf{4.71 \times 10^5}$
25.0	$\mathbf{1.23 \times 10^6}$	2.10×10^6	$\mathbf{1.01 \times 10^6}$	1.62×10^6	$\mathbf{4.42 \times 10^5}$
25.5	$\mathbf{1.29 \times 10^6}$	2.09×10^6	$\mathbf{1.04 \times 10^6}$	1.60×10^6	$\mathbf{4.09 \times 10^5}$
26.0	$\mathbf{1.34 \times 10^6}$	2.08×10^6	$\mathbf{1.07 \times 10^6}$	1.58×10^6	$\mathbf{3.75 \times 10^5}$
26.5	$\mathbf{1.39 \times 10^6}$	2.06×10^6	$\mathbf{1.09 \times 10^6}$	1.56×10^6	$\mathbf{3.42 \times 10^5}$
27.0	$\mathbf{1.43 \times 10^6}$	2.04×10^6	$\mathbf{1.11 \times 10^6}$	1.54×10^6	$\mathbf{3.03 \times 10^5}$
27.5	$\mathbf{1.47 \times 10^6}$	2.02×10^6	$\mathbf{1.13 \times 10^6}$	1.51×10^6	$\mathbf{2.62 \times 10^5}$
28.0	$\mathbf{1.51 \times 10^6}$	2.00×10^6	$\mathbf{1.15 \times 10^6}$	1.48×10^6	$\mathbf{2.21 \times 10^5}$
28.5	$\mathbf{1.54 \times 10^6}$	1.97×10^6	$\mathbf{1.16 \times 10^6}$	1.46×10^6	1.77×10^5
29.0	$\mathbf{1.57 \times 10^6}$	1.94×10^6	$\mathbf{1.17 \times 10^6}$	1.43×10^6	1.28×10^5
29.5	$\mathbf{1.60 \times 10^6}$	1.91×10^6	$\mathbf{1.17 \times 10^6}$	1.39×10^6	8.48×10^4
30.0	$\mathbf{1.63 \times 10^6}$	1.87×10^6	$\mathbf{1.17 \times 10^6}$	1.36×10^6	4.64×10^4
30.5	$\mathbf{1.65 \times 10^6}$	1.83×10^6	$\mathbf{1.18 \times 10^6}$	1.33×10^6	2.06×10^4
31.0	$\mathbf{1.67 \times 10^6}$	1.80×10^6	$\mathbf{1.18 \times 10^6}$	1.29×10^6	7.45×10^3
31.5	$\mathbf{1.68 \times 10^6}$	1.77×10^6	$\mathbf{1.18 \times 10^6}$	1.26×10^6	*0.00*
32.0	$\mathbf{1.69 \times 10^6}$	1.75×10^6	$\mathbf{1.18 \times 10^6}$	1.22×10^6	*0.00*
32.5	$\mathbf{1.70 \times 10^6}$	1.71×10^6	$\mathbf{1.17 \times 10^6}$	1.19×10^6	
33.0	$\mathbf{1.71 \times 10^6}$	1.68×10^6	$\mathbf{1.17 \times 10^6}$	1.16×10^6	
33.5	$\mathbf{1.72 \times 10^6}$	1.64×10^6	$\mathbf{1.16 \times 10^6}$	1.13×10^6	
34.0	$\mathbf{1.72 \times 10^6}$	1.61×10^6	$\mathbf{1.15 \times 10^6}$	1.09×10^6	
34.5	$\mathbf{1.72 \times 10^6}$	1.57×10^6	$\mathbf{1.14 \times 10^6}$	1.06×10^6	
35.0	$\mathbf{1.71 \times 10^6}$	1.53×10^6	1.13×10^6	1.02×10^6	
35.5	1.70×10^6	1.50×10^6	1.11×10^6	9.95×10^5	
36.0	1.69×10^6	1.47×10^6	1.10×10^6	9.38×10^5	
36.5	1.68×10^6	1.44×10^6	1.08×10^6	9.19×10^5	
37.0	1.66×10^6	1.40×10^6	1.07×10^6	8.96×10^5	
37.5	1.64×10^6	1.37×10^6	1.05×10^6	8.50×10^5	
38.0	1.63×10^6	1.33×10^6	1.04×10^6	8.12×10^5	
38.5	1.61×10^6	1.30×10^6	1.03×10^6	7.90×10^5	
39.0	1.60×10^6	1.27×10^6	1.01×10^6	7.41×10^5	
39.5	1.58×10^6	1.24×10^6	9.97×10^5	7.05×10^5	
40.0	1.57×10^6	1.20×10^6	9.81×10^5	6.71×10^5	
40.5	1.55×10^6	1.16×10^6	9.64×10^5	6.48×10^5	
41.0	1.53×10^6	1.12×10^6	9.46×10^5	6.29×10^5	
41.5	1.52×10^6	1.09×10^6	9.26×10^5	5.71×10^5	
42.0	1.50×10^6	1.06×10^6	9.05×10^5	5.54×10^5	
42.5	1.48×10^6	1.04×10^6	8.83×10^5	5.13×10^5	
43.0	1.46×10^6	1.00×10^6	8.60×10^5	4.86×10^5	
43.5	1.44×10^6	9.75×10^5	8.36×10^5	4.40×10^5	
44.0	1.41×10^6	9.46×10^5	8.11×10^5	4.15×10^5	
44.5	1.39×10^6	9.11×10^5	7.87×10^5	3.72×10^5	
45.0	1.36×10^6	8.80×10^5	7.62×10^5	3.55×10^5	
45.5	1.34×10^6	8.48×10^5	7.38×10^5	3.15×10^5	
46.0	1.31×10^6	8.23×10^5	7.14×10^5	2.89×10^5	
46.5	1.28×10^6	7.94×10^5	6.89×10^5	2.45×10^5	

APPENDIX

Continued[a]

Tube	Heliodent[c]	Isovolt[b]	Heliodent[c]	Isovolt[b]	Isovolt[b]
μGy/mAs at 1 m	64.3	121.1	46.7	88	3
EPPT (± 0.1 μm)	1 ± 0.5 μm	0.9 μm	1 ± 0.5 μm	0.8 μm	0.6 μm
keV	70 kVp	60 kVp	60 kVp	50.8 kVp	30.8 kVp
47.0	1.25×10^6	7.68×10^5	6.65×10^5	2.13×10^5	
47.5	1.22×10^6	7.41×10^5	6.40×10^5	*1.82×10^5*	
48.0	1.19×10^6	7.15×10^5	6.15×10^5	*1.34×10^5*	
48.5	1.16×10^6	6.84×10^5	5.89×10^5	*9.60×10^4*	
49.0	1.12×10^6	6.59×10^5	5.62×10^5	*5.61×10^4*	
49.5	1.09×10^6	6.29×10^5	5.36×10^5	*3.18×10^4*	
50.0	1.06×10^6	5.98×10^5	5.09×10^5	*1.51×10^4*	
50.5	1.03×10^6	5.72×10^5	4.82×10^5	*9.68×10^3*	
51.0	9.99×10^5	5.43×10^5	4.54×10^5	*9.69×10^3*	
51.5	9.69×10^5	5.08×10^5	4.27×10^5	*7.75×10^3*	
52.0	9.39×10^5	4.80×10^5	4.01×10^5	*5.82×10^3*	
52.5	9.09×10^5	4.56×10^5	3.74×10^5	*0.00*	
53.0	8.78×10^5	4.29×10^5	3.47×10^5	*0.00*	
53.5	8.47×10^5	4.03×10^5	3.21×10^5		
54.0	8.16×10^5	3.77×10^5	2.95×10^5		
54.5	7.85×10^5	3.48×10^5	2.69×10^5		
55.0	7.54×10^5	3.20×10^5	2.43×10^5		
55.5	7.24×10^5	2.95×10^5	2.18×10^5		
56.0	6.93×10^5	2.64×10^5	1.92×10^5		
56.5	6.61×10^5	2.38×10^5	1.67×10^5		
57.0	6.29×10^5	2.14×10^5	1.44×10^5		
57.5	5.98×10^5	1.82×10^5	1.19×10^5		
58.0	5.68×10^5	*1.50×10^5*	*9.81×10^4*		
58.5	5.38×10^5	*1.16×10^5*	*7.78×10^4*		
59.0	5.08×10^5	*8.87×10^4*	*6.10×10^4*		
59.5	4.78×10^5	*5.80×10^4*	*4.58×10^4*		
60.0	4.49×10^5	*3.01×10^4*	*3.25×10^4*		
60.5	4.22×10^5	*1.03×10^4*	*5.88×10^3*		
61.0	3.93×10^5	*8.72×10^3*	*2.15×10^3*		
61.5	3.68×10^5	*6.00×10^3*	*0.00*		
62.0	3.41×10^5	*0.00*	*0.00*		
62.5	3.14×10^5	*0.00*			
63.0	2.91×10^5				
63.5	2.67×10^5				
64.0	2.45×10^5				
64.5	2.21×10^5				
65.0	1.98×10^5				
65.5	1.78×10^5				
66.0	1.58×10^5				
66.5	1.39×10^5				
67.0	9.78×10^4				
67.5	8.39×10^4				
68.0	*6.94×10^4*				
68.5	*5.66×10^4*				
69.0	*4.29×10^4*				
69.5	*3.25×10^4*				
70.0	*1.66×10^4*				
70.5	*1.66×10^4*				
71.0	*6.19×10^3*				
71.5	*0.00*				
72.0	*0.00*				

[a] Format: absolute fluence primary spectra (X rays/mAs·cm² at 1 m in 0.5-keV energy bins). Data with standard font indicate ±3% error. Data in italics indicate ±10% error. Data in boldface indicate ±5% error.

[b] Seifert Isovolt tube: constant potential, 20° pure tungsten anode. Total filtration: inherent filtration (7 mm beryllium) + effective pitting and plating thickness (listed in μm) + 0.5 mm aluminum.

[c] Siemens Heliodent tube: constant potential, 12° pure tungsten anode. Total filtration: inherent filtration (0.8 mm pyrex glass, 15 mm insulating oil, 1.3 mm aluminum) + effective pitting and plating thickness.

ACKNOWLEDGMENTS

We extend our gratitude to Mr. Dale Thomas, MSgt. Jocelyn Nixon, and Capt. Francis Afinidad of Brooks Air Force Base for unlimited access to their outstanding calibration facility and for use of their germanium detector, nuclear instrument modules, oscilloscope, and primary standard ion chamber. We thank Maj. Casmere Taylor, Maj. Walt Loring, and Sgt. Porter Burnett of Brooks Army Medical Center for loan of their cadmium-zinc-telluride detector and multichannel analyzer. We also thank Professor Gary Fullerton and Dr. Randy Glickman of The University of Texas Health Science Center at San Antonio for loan of the MDH monitor and various optics components.

Received: July 19, 1999; accepted: April 30, 2000

REFERENCES

1. A. E. Profio, Ed., *Shielding Benchmark Problems.* Publication ORNL-RSIC-25, Oak Ridge National Laboratory, Oak Ridge, TN, 1969.
2. M. Bhat, J. Pattison, G. Bibbo and M. Caon, Diagnostic X-ray spectra: A comparison of spectra generated by different computational methods with a measured spectrum. *Med. Phys.* **25**, 114–120 (1998).
3. E. R. Epp and H. Weiss, Experimental study of the photon energy spectrum of primary diagnostic x-rays. *Phys. Med. Biol.* **11**, 225–238 (1966).
4. T. R. Fewell and R. E. Shuping, Photon energy distribution of some typical diagnostic x-ray beams. *Med. Phys.* **4**, 187–197 (1977).
5. T. R. Fewell, R. E. Shuping and K. R. Hawkins, *Handbook of Computed Tomography X-Ray Spectra.* Publication HHS (FDA) 81–8162, U.S. Government Printing Office, Washington, DC, 1981.
6. G. Hettinger and N. Starfelt, Bremsstrahlung spectra from Roentgen tubes. *Acta Radiol.* **50**, 381–394 (1958).
7. H. I. Israel, D. W. Lier and E. Storm, Comparison of detectors used in measurement of 10 to 300 keV X-ray spectra. *Nucl. Instrum. Methods* **91**, 141–157 (1971).
8. M. Marshall, L. H. Peaple, G. M. Ardran and H. E. Crook, A comparison of x-ray spectra and outputs from molybdenum and tungsten targets. *Br. J. Radiol.* **48**, 31–39 (1975).
9. L. H. Peaple and A. K. Burt, The measurement of spectra from x-ray machines. *Phys. Med. Biol.* **14**, 73–85 (1969).
10. W. W. Seelentag and W. Panzer, Stripping of X-ray bremsstrahlung spectra up to 300 kVp on a desk type computer. *Phys. Med. Biol.* **24**, 767–780 (1979).
11. E. Storm, H. I. Israel and D. W. Lier, *Bremsstrahlung Emission Measurement for Thick Tungsten Targets in the Energy Range 12 to 300 kV.* Publication LA-4624, Los Alamos National Laboratory, Los Alamos, NM, 1971.
12. R. G. Waggener, L. B. Levy, L. F. Rogers and P. Zanca, Measured X-ray spectra from 25 to 110 kVp for a typical diagnostic unit. *Radiology* **105**, 169–175 (1972).
13. J. W. Boag, Ionization chambers. In *Radiation Dosimetry, Vol. II—Instrumentation*, 2nd ed. (F. H. Attix and E. Tochilin, Eds.), pp. 54–55. Academic Press, New York, 1966.
14. T. R. Lee, *Evaluation of MDH 1015 X-Ray Monitor.* Publication HEW (FDA) 77-8014, U.S. Government Printing Office, Washington, DC, 1977.
15. S. M. Seltzer, Calculated response of intrinsic germanium detectors to narrow beams of photons with energies up to ~300 keV. *Nucl. Instrum. Methods* **188**, 133–151 (1981).
16. J. F. Briesmeister, Ed., *MCNP—A General Monte Carlo N-Particle Transport Code, Version 4B.* ORNL RSICC Computer Code Collection CD-ROM # MCNP4B2, Los Alamos National Laboratory, Los Alamos, NM, 1997.
17. *LLNL Libraries of Atomic Data, Electron Data, and Photon Data in Evaluated Nuclear Data Library* (*ENDL*) *Type Format.* ORNL RSICC Data Library Collection CD-ROM # ENDLIB-97, Oak Ridge National Laboratory, Oak Ridge, TN, 1997.
18. P. J. Lamperti, T. P. Loftus and R. Loevinger, *Calibration of X-Ray and Gamma-Ray Measuring Instruments.* NBS Special Publication 250-16, National Bureau of Standards, Gaithersburg, MD, 1988.
19. G. D. Fullerton and R. Gragg, Calibration of Medium-Energy X-Ray Units (20–300 kV). In *Handbook of Medical Physics*, Vol. I (R. G. Waggener, J. G. Kereiakes and R. J. Shalek, Eds.), pp. 103–117. CRC Press, Boca Raton, FL, 1982.
20. F. H. Attix, *Introduction to Radiological Physics and Radiation Dosimetry.* Wiley, New York, 1986.
21. J. H. Hubbell and S. M. Seltzer, *Tables of X-Ray Mass Attenuation and Mass Energy-Absorption Coefficients 1 keV to 20 MeV for Elements Z-1 to 92 and 48 Additional Substances of Domestic Interest.* Publication NISTIR 5632, National Institute of Standards and Technology, Gaithersburg, MD, 1995.
22. H. A. Kramers, On the theory of X-ray absorption and of the continuous X-ray spectrum. *Phil. Mag.* **46**, 836–871 (1923).